Direct Current Tracking Using Boundary Control With Second-Order Switching Surface for Three-Phase Three-Wire Grid-Connected Inverter

Yuanbin He, *Student Member, IEEE*, Henry Shu-hung Chung, *Fellow, IEEE*, Carl Ngai-Man Ho, *Senior Member, IEEE*, and Weimin Wu

***Abstract*—Cascaded boundary-deadbeat controller can ensure system stability of single-phase grid-connected inverter operated under different grid conditions. However, it will require using numerous sensors and may experience performance degradation caused by unbalanced filter parameters in controlling a three-phase three-wire inverter. Furthermore, the system is in variable frequency operation. A boundary controller using second-order switching surface with direct current tracking capability, reduced number of current sensors, and fixed frequency operation of three-phase three-wire grid-connected inverter with inductive-capacitive-inductive (*LCL*) filter is presented. By applying the 60° discontinuous pulsewidth modulation scheme for a fictitious decoupled dual-buck structure in each operation sector, two separate sets of switching criteria for dictating the states of the switches of two half-bridge legs are formulated. Such technique can avoid dealing with the challenges caused by the interactions among three independent current regulators. A switching table with null voltage vectors excluded is designed to dictate the switching actions. Sensitivities of the system transfer characteristics to the parametric variations are investigated. A 3 kW prototype has been built and evaluated under stiff- and weak-grid conditions. The experimental results are favorably compared with theoretical predictions.**

***Index Terms*—Boundary control, dc–ac power conversion, fictitious decoupled dual-buck converter, *LCL* filter, second-order switching surface, three-phase inverters.**

I. Introduction

MODERN grid-connected voltage source inverters (VSIs) are required to assure its system stability under different grid conditions, while high-order output filters, such as *LCL* filter, are used to minimize their physical size [1]. They are necessary to deal with many intrinsic and extrinsic challenges, such as oscillation due to filter resonance, uncertainty of the grid condition, disturbances at the point of common coupling (PCC), etc. Many prior arts, such as passive and active damping techniques [2]–[10], have been proposed to tackle filter resonance. Among them, active damping techniques are popular, as they do not cause extra power loss and can adjust the damping factor flexibly on digital controller. However, their performance would sometimes degrade if the inverter is operated under weak grid condition [11]. The resonance frequency will vary as the grid-impedance changes. Thus, many improved solutions, such as hybrid damping methods [12], active damping with reduced computational delay [13], and active damper installed at the PCC [14], have been proposed to deal with the impact of the grid impedance on the system performance. However, disturbances at the PCC caused by the source or nonlinear loads would sometimes affect their normal operations. Inverter with slow dynamics or poor harmonic suppression would deteriorate voltage distortion at the PCC [15]. Selective harmonic compensators and grid-impedance estimation algorithm are usually used to alleviate such issue [16]–[20]. Thus, many performance and design tradeoffs have to be made in designing above-mentioned controllers.

Considering that nonlinear boundary control techniques usually exhibit high operational stability under wide parametric variations and superior dynamic behaviors, they would be favorable in meeting the above-mentioned requirements. With the recent advances in microelectronics and digital controllers, more and more digital boundary control methods have been reported [21], [22], [26], [29]–[31], [41]. They include hysteresis current control (HCC), direct power control (DPC), sliding mode control (SMC), and boundary control with second-order switching surface (BC2), to program the output current of grid-connected VSIs. Their operating principle is based on guiding the state variables to move along a predefined linear or curved switching surface.

The HCC involves simple operations by guiding the inverter output current to move along the predefined target point or surface. It exhibits precise current tracking performance and superior stability. To mitigate filter resonance, integration of active damping techniques is needed [21]–[24]. As the intracycle information of the state variables is included in the damping function, it would interfere with the predefined switching

Manuscript received April 9, 2016; revised July 8, 2016; accepted August 26, 2016. Date of publication September 12, 2016; date of current version February 27, 2017. This work was supported by the Research Grants Council of the Hong Kong Special Administrative Region, China, under NSFC/RGC Joint Research Scheme Project: N_CityU128/15 and Project 51561165013. This paper was presented in part at the *IEEE Energy Conversion Congress and Exposition* (ECCE) 2016. Recommended for publication by Associate Editor S. Kapat.

Y. He and H. S.-H. Chung are with the Centre for Smart Energy Conversion and Utilization Research, City University of Hong Kong, Kowloon Tong, Hong Kong (e-mail: yuanbinhe2-c@my.cityu.edu.hk; eeshc@cityu.edu.hk).

C. N.-M. Ho is with the Department of Electrical & Computer Engineering, University of Manitoba, Winnipeg, MB R3T 5V6, Canada (e-mail: carl.ho@umanitoba.ca).

W. Wu is with the Research Institute of Electronic Automation, Shanghai Maritime University, Shanghai 201306, China (e-mail: wmwu@shmtu.edu.cn).

Color versions of one or more of the figures in this paper are available online at http://ieeexplore.ieee.org.

Digital Object Identifier 10.1109/TPEL.2016.2608355

surface and thus tradeoff design should be taken. The DPC utilizes the instantaneous output power information by multiplying the output voltage and current of the inverter to regulate the switching states through a switching table [25]. However, the product of the output current and voltage would lose the phase information, intracycle information and even magnitude information especially at near zero-cross point of them. Thus, integration of the active damping function is also needed for dealing with filter resonance [26]–[28]. The SMC usually utilizes linear switching surface by composing the system state variables and references to dictate the states of the switches [29]–[31]. It exhibits the filter resonance mitigation capability, high operational stability, and good harmonic suppression. However, its output current tracking performance is susceptible to the drift of circuit parameters. Thus, an additional integral or resonant term of the state variables is usually introduced into the sliding function to improve current tracking [31], [32].

The BC2 exploits second-order or curved switching surfaces for the state variables to dictate the states of the switches [33]. It was followed by the development of the high-order switching surface [34] and natural switching surface [35], exhibiting enhanced dynamic performance at start-up and under large-signal transients. They have been proven to outperform the SMC with linear switching surface, in terms of the settling time, steady-state error, and dynamic response [36]. Such fast dynamic control concept has been attempted in controlling off-grid inverters [34], [37], [38] and boost-type power factor (PF) correctors [39], [40]. Recently, the BC2 has been extended to single-phase grid-connected inverter with *LCL* filter by cascading a deadbeat current controller (DBC) to regulate the grid current [41]. The structure hybridizes the merits of the DBC for its simplicity in the implementation and the BC2 for its superior fast dynamics. It is proven that the BC2 avoids filter resonance and the DBC advances the performance characteristics of the inverter under different grid conditions. However, apart from requiring numerous sensors and dealing with challenges caused by unbalanced filter parameters, the cascaded BC2–DBC scheme also operates in variable switching frequency, due to coupling circuit variables amongst phases, in controlling three-phase three-wire inverter.

This paper will present a BC2 with:

1) direct current tracking capability;
2) reduced number of current sensors;
3) fixed frequency operation for three-phase three-wire grid-connected inverter with *LCL* filter.

It retains the merits of performing wide control bandwidth and high operational stability under different grid conditions. By applying the 60° discontinuous pulsewidth modulation (60° DPWM) scheme for a fictitious decoupled dual-buck structure in each operation sector, two separate sets of the switching criteria with fixed frequency operation for dictating the states of the switches of two half-bridge legs are formulated. The tracking error of the injected current is minimized by feedforwarding the capacitor current error. A switching table with null voltage vectors excluded is designed to dictate the switching actions to alleviate common-mode voltage. The effect of unbalanced filter parameters on the transfer characteristics of the entire inverter system will be investigated. A 3-kW prototype has been built and evaluated.

II. Derivation of a Fictitious Dual-Buck Structure With 60° DPWM

Three-phase two-level grid-connected VSI has been commonly used in medium-power applications [11]. As shown in Fig. 1, the equivalent PCS of a typical three-phase two-level grid-connected VSI consists of a switching network and an output *LCL* filter. L_1, L_2, and C_f are the inverter-side filter inductor, grid-side filter inductor or the leakage inductance of the isolating transformer, and filter capacitor, respectively. L_g represents equivalent grid inductance. For simplicity, the filter parameters amongst phases are assumed to be balanced. Thus, the inverter is modeled by the state-space equations of

$$\begin{bmatrix} \dot{i}_{1,A} \\ \dot{i}_{1,B} \\ \dot{i}_{1,C} \end{bmatrix} = \frac{1}{L_1} \left\{ \begin{bmatrix} u_{1,\mathrm{Ao}} \\ u_{1,\mathrm{Bo}} \\ u_{1,\mathrm{Co}} \end{bmatrix} - \begin{bmatrix} u_{C,\mathrm{Ao}} \\ u_{C,\mathrm{Bo}} \\ u_{C,\mathrm{Co}} \end{bmatrix} \right\} \tag{1a}$$

$$\begin{bmatrix} \dot{u}_{C,\mathrm{Ao}} \\ \dot{u}_{C,\mathrm{Bo}} \\ \dot{u}_{C,\mathrm{Co}} \end{bmatrix} = \frac{1}{C_f} \begin{bmatrix} i_{C,A} \\ i_{C,B} \\ i_{C,C} \end{bmatrix} \tag{1b}$$

$$\begin{bmatrix} \dot{i}_{g,A} \\ \dot{i}_{g,B} \\ \dot{i}_{g,C} \end{bmatrix} = \frac{1}{L_2 + L_g} \left\{ \begin{bmatrix} u_{C,\mathrm{Ao}} \\ u_{C,\mathrm{Bo}} \\ u_{C,\mathrm{Co}} \end{bmatrix} - \begin{bmatrix} u'_{g,\mathrm{Ao}} \\ u'_{g,\mathrm{Bo}} \\ u'_{g,\mathrm{Co}} \end{bmatrix} \right\} \tag{1c}$$

where the neutral point of filter capacitors "*o*" is assumed to be the common reference point.

Due to the three-wire configuration, the voltage and current information in (1) is cross-coupled. By using three separate sets of cascaded BC2–DBC with such coupling phase information directly as presented in [41], it would introduce interference in predicting the state trajectories and lead to wide variation of switching frequency. In order to decouple the circuit variables amongst phases for the BC2 operation, a fictitious dual-buck structure with 60° DPWM is proposed in the following.

The operation of the switching network is divided into six sectors over a line cycle. Such 60° DPWM is depicted in Fig. 2 [42]. Each sector has the switches of two half-bridge legs in high-frequency switching. For example, the terminal voltage $u_{g,\mathrm{Bo}}$ or the inverter output voltage $u_{1,\mathrm{Bo}}$ is the lowest in Sector II. Thus, S_{bn} is ON and S_{bp} is OFF. The switch pairs (S_{ap}, S_{an}) and $(S_{\mathrm{cp}}, S_{\mathrm{cn}})$ in the other two half-bridge legs are switched complementally. In order to avoid actual measurement of the inverter output voltage, the grid voltage is used to define the operation sector. Minor phase difference between the inverter output voltage and grid voltage is allowed [42]. Fig. 3(a) shows the simplified circuit when the inverter is in Sector II.

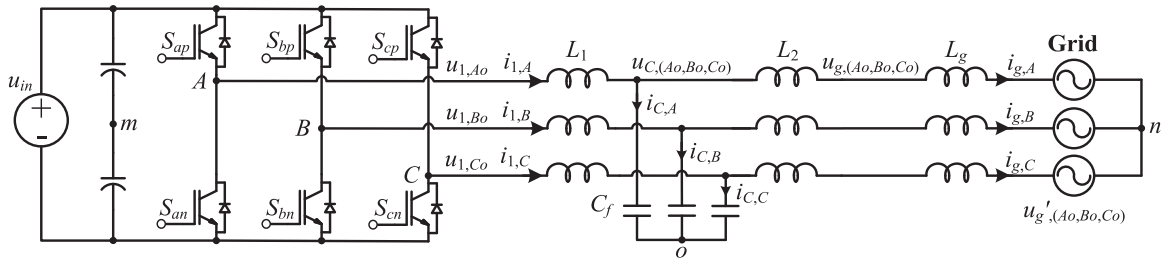

Fig. 1. PCS of three-phase two-level grid-connected inverter.

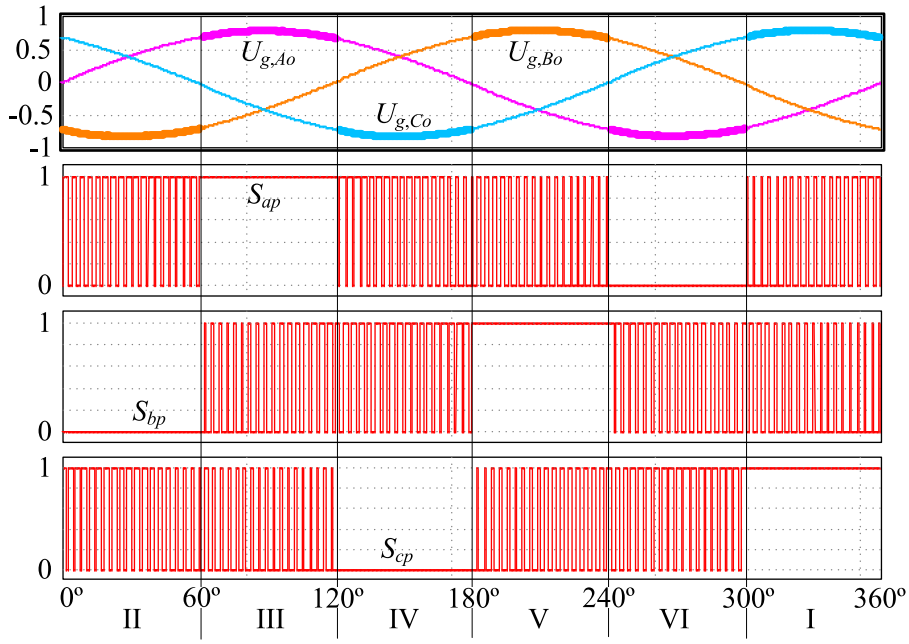

Fig. 2. Principle of 60° DPWM.

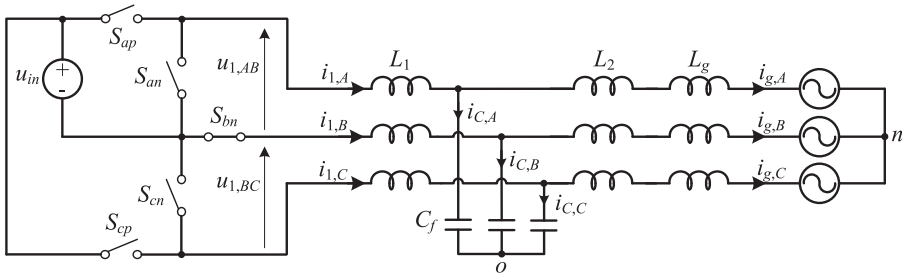

(a)

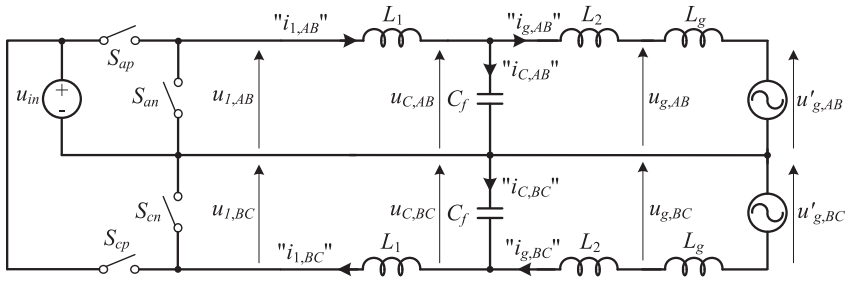

(b)

Fig. 3. Derivation of the fictitious DM decoupled dual-buck structure in Sector II. (a) Simplified circuit, (b) fictitious DM decoupled equivalent circuit.

Let $i_{C,\mathrm{AB}} = i_{C,A} - i_{C,B}$ and $u_{C,\mathrm{AB}} = u_{C,\mathrm{Ao}} - u_{C,\mathrm{Bo}}$, (1) can be rewritten as

$$\begin{bmatrix} \dot{i}_{1,\mathrm{AB}} \\ \dot{i}_{1,\mathrm{BC}} \\ \dot{i}_{1,\mathrm{CA}} \end{bmatrix} = \begin{bmatrix} \dot{i}_{1,A} - \dot{i}_{1,B} \\ \dot{i}_{1,B} - \dot{i}_{1,C} \\ \dot{i}_{1,C} - \dot{i}_{1,A} \end{bmatrix} = \frac{1}{L_1} \left\{ \begin{bmatrix} u_{1,\mathrm{AB}} \\ u_{1,\mathrm{BC}} \\ u_{1,\mathrm{CA}} \end{bmatrix} - \begin{bmatrix} u_{C,\mathrm{AB}} \\ u_{C,\mathrm{BC}} \\ u_{C,\mathrm{CA}} \end{bmatrix} \right\} \tag{2a}$$

$$\begin{bmatrix} \dot{u}_{C,\mathrm{AB}} \\ \dot{u}_{C,\mathrm{BC}} \\ \dot{u}_{C,\mathrm{CA}} \end{bmatrix} = \frac{1}{C_f} \begin{bmatrix} i_{C,A} - i_{C,B} \\ i_{C,B} - i_{C,C} \\ i_{C,C} - i_{C,A} \end{bmatrix} = \frac{1}{C_f} \begin{bmatrix} i_{C,\mathrm{AB}} \\ i_{C,\mathrm{BC}} \\ i_{C,\mathrm{CA}} \end{bmatrix} \tag{2b}$$

$$\begin{bmatrix} \dot{i}_{g,\mathrm{AB}} \\ \dot{i}_{g,\mathrm{BC}} \\ \dot{i}_{g,\mathrm{CA}} \end{bmatrix} = \begin{bmatrix} \dot{i}_{g,A} - \dot{i}_{g,B} \\ \dot{i}_{g,B} - \dot{i}_{g,C} \\ \dot{i}_{g,C} - \dot{i}_{g,A} \end{bmatrix} = \frac{1}{L_2 + L_g} \left\{ \begin{bmatrix} u_{C,\mathrm{AB}} \\ u_{C,\mathrm{BC}} \\ u_{C,\mathrm{CA}} \end{bmatrix} - \begin{bmatrix} u'_{g,\mathrm{AB}} \\ u'_{g,\mathrm{BC}} \\ u'_{g,\mathrm{CA}} \end{bmatrix} \right\}. \tag{2c}$$

It should be noted that the conversion given in (2), i.e., $i_{1,\mathrm{AB}} = i_{1,A} - i_{1,B}$, is purely a mathematical model without physical interpretation. Such current subtraction is specifically used to decouple the current regulation in the proposed control scheme. Based on (2), a fictitious decoupled differential-mode (DM) parallel-connected dual-buck converter structure, as shown in Fig. 3(b), can be derived. Similar fictitious circuit structures can be derived for the rest of five sectors.

Define that the switching function of the switching network is

$$SW_k|_{k=a,b,\mathrm{or},c} = \begin{cases} 1 & S_{\mathrm{kp}} \text{ is on and } S_{\mathrm{kn}} \text{ is off} \\ 0 & S_{\mathrm{kp}} \text{ is off and } S_{\mathrm{kn}} \text{ is on} \end{cases}. \tag{3}$$

Thus, there are eight possible inverter output voltage vectors, $\vec{U}_0 = [0\ \ 0\ \ 0], \ldots,$ and $\vec{U}_7 = [1\ \ 1\ \ 1]$, corresponding to eight states $\vec{S}_l = (\mathrm{SW}_a\mathrm{SW}_b\mathrm{SW}_c), l = 0, 1, \ldots, 7$, in which six are active vectors and the other two are null vectors, and '1' and '0' denote $u_{\mathrm{in}}/2$ and $-u_{\mathrm{in}}/2$ at the inverter output with reference to the mid-point '*m*' of the dc bus, respectively. To reduce the common-mode voltage (CMV), null vectors, including $\vec{U}_0$ and $\vec{U}_7$, with relatively high CMV are usually avoided [43].

III. Current-Mode BC2 for the Fictitious Dual-Buck Structure

Based on the fictitious dual-buck structure shown in Fig. 3(b), two sets of BC2 switching criteria, one for each half-bridge leg, are derived in this section. Each set includes two equations to define the states of the switches in one leg. The formulated BC2 with reduced current sensing and fixed frequency operation is in current mode and will track the grid current directly without extra current regulation control.

Fig. 4 shows the architecture of the whole system, in which the inverter-side inductor current $i_{1,k}$, filter capacitor voltage $u_{C,ko}$, and grid voltage $u_{g,ko}$ are sensed by the controller, i and j represent the labels AB, BC, or CA based on the result of data mapping, P_{ref} and Q_{ref} are the active and reactive reference power to generate reference current, $i_{g,\mathrm{ref},i}$ and $i_{g,\mathrm{ref},j}$, and phase angle θ_g is given by the phase locked loop.

A. Derivation of the Switching Criteria With BC2

Fig. 5 shows the intracycle information between the fictitious decoupled filter capacitor current $i_{C,i}$ and capacitor voltage $u_{C,i}$, where $i = AB, BC$, or *CA*. $u_{\mathrm{ref},i}$ and $i_{C,\mathrm{line},i}$ are the line-frequency components of $u_{C,i}$ and $i_{C,i}$, respectively. t_1, t_2, and t_3 are switching instants. t_1^+ and t_2^+ are the time instants infinitesimally after t_1 and t_2, respectively. Based on the derivation in Appendix A, the switching criteria for tracking the reference voltage $u_{\mathrm{ref},i}$ are

$$\sigma_{i-}^2 = K_{i,1}(t)[u_{C,i}(t) - u_{\mathrm{ref},i}(t)] - K_0[i_{C,i}(t)^2 - \Delta I_{-,i}(t)^2] \tag{4a}$$

$$\sigma_{i+}^2 = K_{i,2}(t)[u_{C,i}(t) - u_{\mathrm{ref},i}(t)] - K_0[i_{C,i}(t)^2 - \Delta I_{+,i}(t)^2] \tag{4b}$$

where $K_{i,1}$ and $K_{i,2}$ are instantaneous voltage information across the inverter-side inductor during Mode-1 (σ_{i-}^2) and Mode-2 (σ_{i+}^2) operations, $K_0 = L_1/(2C_f)$ are the control parameters determined by the nominal values of filter parameters, $\Delta I_{-,i} = i_{C,\mathrm{line},i} - \Delta i_{C,i}$ and $\Delta I_{+,i} = i_{C,\mathrm{line},i} + \Delta i_{C,i}$, and $\Delta i_{C,i}$ is the hysteresis band of the capacitor current.

The switching criteria in (4) are used to regulate $u_{C,i}$ at the reference voltage $u_{\mathrm{ref},i}$. In [41], a DBC is cascaded with the BC2 to perform current tracking function. That is, the DBC generates $u_{\mathrm{ref},i}$ for the BC2 to regulate $u_{C,i}$, so as to track the grid current. However, it requires additional sensor for sensing the grid current.

To eliminate sensing of the capacitor current and grid current, and regulate the grid current, eq. (4) is modified as follows. $i_{C,i}$ and $u_{\mathrm{ref},i}$ can be expressed as

$$i_{C,i}(t) \cong i_{C,i}^*(t) = i_{1,i}(t) - i_{g,\mathrm{ref},i}(t) + e_i(t) = i_{1,i}(t) - i_{g,\mathrm{ref},i}^*(t) \tag{5a}$$

$$u_{\mathrm{ref},i}(t) = u_{g,i}(t) + L_2[i_{g,\mathrm{ref},i}^*(t)]' \tag{5b}$$

where $i_{g,\mathrm{ref},i}$ is the grid current reference, $i_{g,\mathrm{ref},i}^* = i_{g,\mathrm{ref},i} - e_i$ is the corrected reference, and e_i is the line-frequency components of the filter capacitor current error. Thus, the modified grid current command $i_{g,\mathrm{ref},i}^*$ only includes the line frequency component and its derivative in (5b) will not lead to noise amplification. e_i is calculated by using the formula of

$$e_i(t) = i_{C,\mathrm{line},i}^*(t) - i_{C,\mathrm{line},i}(t) \tag{6}$$

where $i_{C,\mathrm{line},i}^*$ is the line-frequency component of the estimated capacitor current, $(i_{1,i} - i_{g,\mathrm{ref},i}^*)$. It can be extracted readily by using a digital band-pass filter. $i_{C,\mathrm{line},i}$ is the calculated value extracted by differentiating the line-frequency component of $u_{C,i}$. It should be noted that it is also possible to obtain $i_{C,\mathrm{line},i}$ by differentiating the low-pass filtered component of $u_{C,i}$ but it might lead to noise amplification and phase delay.

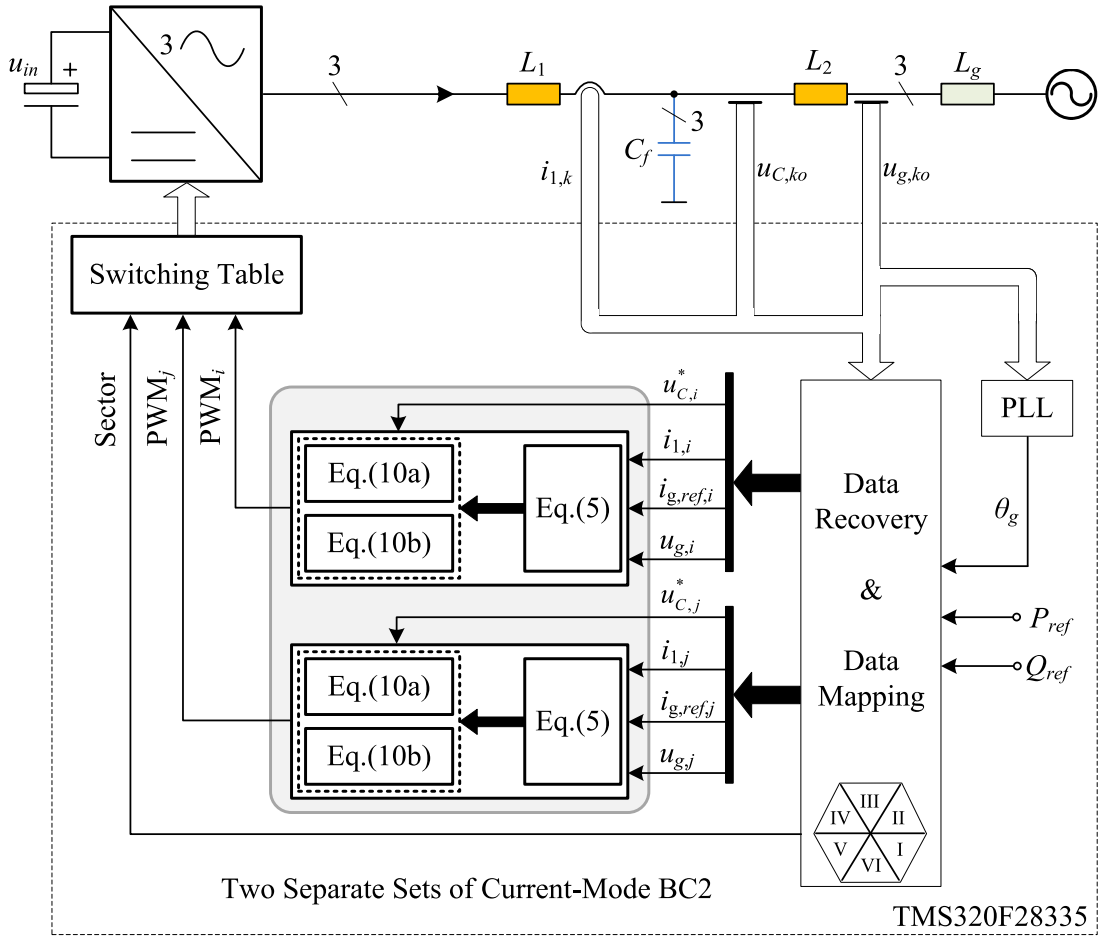

Fig. 4. Architecture of the whole system.

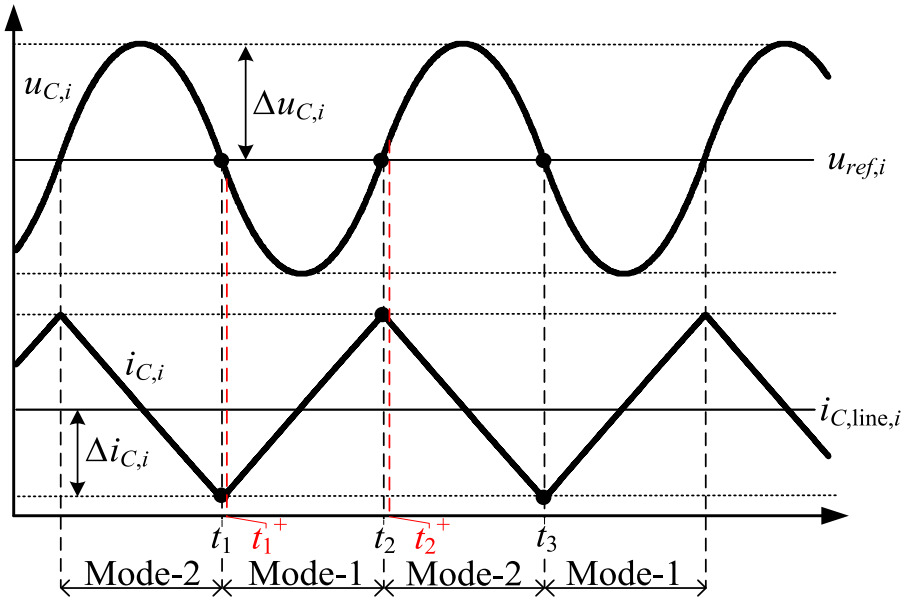

Fig. 5. Typical intracycle waveforms and timing for $u_{C,i}$ and $i_{C,i}$.

TABLE I
$K_{i,1}$ AND $K_{i,2}$ IN DIFFERENT SECTORS

		$K_{i,1}$	$K_{i,2}$
Sector I	$i = BC$	$-u_{C,BC}$	$-u_{in}-u_{C,BC}$
	$i = CA$	$u_{in}-u_{C,CA}$	$-u_{C,CA}$
Sector II	$i = AB$	$u_{in}-u_{C,AB}$	$-u_{C,AB}$
	$i = BC$	$-u_{C,BC}$	$-u_{in}-u_{C,BC}$
Sector III	$i = AB$	$u_{in}-u_{C,AB}$	$-u_{C,AB}$
	$i = CA$	$-u_{C,CA}$	$-u_{in}-u_{C,CA}$
Sector IV	$i = BC$	$u_{in}-u_{C,BC}$	$-u_{C,BC}$
	$i = CA$	$-u_{C,CA}$	$-u_{in}-u_{C,CA}$
Sector V	$i = AB$	$-u_{C,AB}$	$-u_{in}-u_{C,AB}$
	$i = BC$	$u_{in}-u_{C,BC}$	$-u_{C,BC}$
Sector VI	$i = AB$	$-u_{C,AB}$	$-u_{in}-u_{C,AB}$
	$i = CA$	$u_{in}-u_{C,CA}$	$-u_{C,CA}$

By putting (5) and (6) into (4), switching criteria that can directly track the grid current are

$$\sigma_{i-}^2 = K_{i,1}(t)\{u_{C,i}(t) - u_{g,i}(t) - L_2[i_{g,\mathrm{ref},i}^*(t)]'\} - K_0\{[i_{1,i}(t) - i_{g,\mathrm{ref},i}^*(t)]^2 - \Delta I_{-,i}(t)^2\} \quad (7a)$$

$$\sigma_{i+}^2 = K_{i,2}(t)\{u_{C,i}(t) - u_{g,i}(t) - L_2[i_{g,\mathrm{ref},i}^*(t)]'\} - K_0\{[i_{1,i}(t) - i_{g,\mathrm{ref},i}^*(t)]^2 - \Delta I_{+,i}(t)^2\} \quad (7b)$$

where the switching actions of Mode-1 and Mode-2 are specific to a half-bridge leg and sector. For example, in Sector II, the switching state in leg b is maintained at $\mathrm{SW}_b = 0$. Thus, by using circuit variables with $i = AB$ for leg a and $i = BC$ for leg c, two sets of switching criteria in (7) are used to dictate the switching actions of legs a and c, respectively, in which two sets of σ_{i-}^2 are employed for Mode-1 operation and two sets of σ_{i+}^2 are employed for Mode-2 operation. For leg a, Mode-1 operation corresponds to $\mathrm{SW}_a = 1$ and Mode-2 operation corresponds to $\mathrm{SW}_a = 0$. Conversely, for leg c, Mode-1 operation corresponds to $\mathrm{SW}_c = 0$, while Mode-2 operation corresponds to $\mathrm{SW}_c = 1$. Moreover, different sectors and half-bridge legs have different values of $K_{i,1}(t)$ and $K_{i,2}(t)$. Table I tabulates the values of them in each sector.

By comparing (7) with (4), it can be observed that the capacitor current $i_{C,i} = i_{1,i} - i_{g,i}$ has been replaced by the estimated one $i_{C,i}^* = i_{1,i} - i_{g,\mathrm{ref},i}^*$ in (5a) and the capacitor voltage reference $u_{\mathrm{ref},i}$ is calculated by differentiating the current reference $i_{g,\mathrm{ref},i}^*$ in (5b). Thus, the grid current $i_{g,i}$ can be regulated at $i_{g,\mathrm{ref},i}^*$ (or $i_{g,\mathrm{ref},i}$) indirectly by regulating the filter capacitor voltage $u_{C,i}$ at $u_{\mathrm{ref},i}$. Moreover, to minimize the error between i_g and $i_{g,\mathrm{ref}}$ caused by such tolerance, an error signal, e_i, between the low-frequency component of i_C^* and the low-frequency component of i_C, as shown in (6), has been feedforwarded to modify the grid current reference $i_{g,\mathrm{ref}}$ to be $i_{g,\mathrm{ref},i}^*$, as presented in (5a), until e_i tends to zero. Therefore, the new switching criteria can track the grid current to the reference $i_{g,\mathrm{ref},i}^*$ (or $i_{g,\mathrm{ref},i}$) indirectly without additional current regulation. In other words, the proposed BC2 has become a current-mode control scheme, while the traditional BC2 is in voltage-mode control. In (7), inverter-side currents $i_{1,i}$ are measured, so they can also be used for protection purpose.

Based on the fictitious decoupled converter structure in Fig. 3(b), the controlled circuit variables are decoupled. Thus, the switching frequency is regulated by adjusting the bands $\Delta I_{-,i} = i_{C,\mathrm{line},i} - \Delta i_{C,i}$ and $\Delta I_{+,i} = i_{C,\mathrm{line},i} + \Delta i_{C,i}$, in which $\Delta i_{C,i}$ is approximated by

$$\Delta i_{C,i} \cong \Delta i_{1,i} \cong \frac{1}{2L_1 f_{\mathrm{SW}} u_{\mathrm{in}}}(u_{\mathrm{in}}|u_{C,i}| - {u_{C,i}}^2) \quad (8)$$

where f_{SW} is the switching frequency. Hence, f_{SW} can be regulated readily by using u_{in} and $u_{C,i}$ to adjust $\Delta i_{1,i}$.

B. Intracycle Information Recovery Mechanism for $u_{C,i}$

Small intracycle information of the filter capacitor voltage $u_{C,i}$ in (7) is easily contaminated with undesired noises and quantization errors in the sampling process. Thus, the distorted intracycle information introduces inaccuracies in estimating or predicting the state trajectories. To lessen such distortion, a recovery mechanism for the intracycle information of the filter capacitor voltage is proposed.

Based on (5a)

$$u_{C,i}(t) = \frac{1}{C_f}\int i_{C,i}(t)\,dt \cong \frac{1}{C_f}\int [i_{1,i}(t) - i_{g,\mathrm{ref},i}^*(t)]dt. \quad (9)$$

By performing an integration of the high-frequency component of $(i_{1,i} - i_{g,\mathrm{ref},i}^*)$, the intracycle information of $u_{C,i}$ can be extracted. The low-frequency component of $u_{C,i}$ can be sensed by a voltage sensor. Fig. 6 shows the mechanism of extracting the intracycle information. A high-pass filter (HPF) is first used to extract the high-frequency component of the estimated capacitor current $i_{C,i}^* = i_{1,i} - i_{g,\mathrm{ref},i}^*$. Then, its output is integrated by using (9) with the nominal value of $C_f, C_{f,N}$, to derive the high-frequency component of $u_{C,i}, u_{C,\mathrm{HF},i}$. $u_{C,\mathrm{HF},i}$ is passed to a loop to combine it with the low-frequency components of $u_{C,i}, u_{C,\mathrm{LF},i}$, to generate the estimated value of $u_{C,i}, u_{C,i}^*$. $u_{C,\mathrm{LF},i}$ is obtained by integrating the error, $e_{v,i}$, between $u_{C,i}^*$ and $u_{C,i}$. In Fig. 6, the intracycle information of $u_{C,i}$ is retained by differentiating the estimated capacitor current $i_{C,i}^*$, while the integrator performs like a low-pass filter to mitigate noise interference. As the integration time constant T_{in} increases, the noise level can be mitigated.

Thus, by replacing $u_{C,i}$ with $u_{C,i}^*$ in (7), the switching criteria become

$$\sigma_{i-}^2 = K_{i,1}(t)\{u_{C,i}^*(t) - u_{g,i}(t) - L_2[i_{g,\mathrm{ref},i}^*(t)]'\} - K_0\{[i_{1,i}(t) - i_{g,\mathrm{ref},i}^*(t)]^2 - \Delta I_{-,i}(t)^2\} \quad (10a)$$

$$\sigma_{i+}^2 = K_{i,2}(t)\{u_{C,i}^*(t) - u_{g,i}(t) - L_2[i_{g,\mathrm{ref},i}^*(t)]'\} - K_0\{[i_{1,i}(t) - i_{g,\mathrm{ref},i}^*(t)]^2 - \Delta I_{+,i}(t)^2\}. \quad (10b)$$

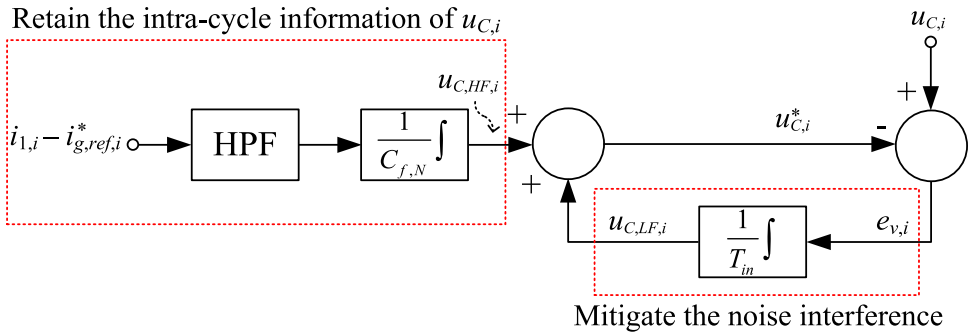

Fig. 6. Mechanism for recovering the intracycle information of $u_{C,i}$.

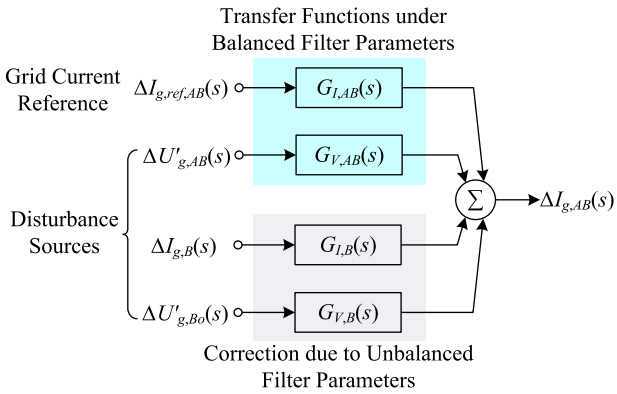

Fig. 7. MIMO inverter system under the condition of unbalanced filter parameters.

C. Switching Table for the BC2 With Null Vectors Excluded

As shown in Fig. 4, the control commands generated by the BC2 are mapped into corresponding sectors before feeding into the driving signals through a switching table. Moreover, considering the effect of the CMV, null vectors, including $\vec{U}_0$ and $\vec{U}_7$, should be avoided [43]. Therefore, a switching table for the proposed current-mode BC2 with null vectors excluded is tabulated as shown in Table II and null vectors are replaced with adjacent active vectors. In the table, '1' or '0' for $i^*_{C,i}(i^*_{C,j})$, $\sigma^2_{i-}(\sigma^2_{i+})$ and $\sigma^2_{j-}(\sigma^2_{j+})$ denote the value larger or smaller than zero, which dictates the switching states specific to a half-bridge leg and sector. For example, in Sector II, the switching state in leg b is maintained at $\mathrm{SW}_b = 0$. Switches in legs a and c are regulated based on two separate sets of switching criteria, $\sigma^2_{i-}(\sigma^2_{i+})$ and $\sigma^2_{j-}(\sigma^2_{j+})$, with $i = AB$ and $j = BC$, respectively. Switching criteria σ^2_{i-} and σ^2_{j-} of Mode-1 operation are used only when $\mathrm{sgn}(i^*_{C,i}) = 0$ and $\mathrm{sgn}(i^*_{C,j}) = 0$, respectively. Similarly, switching criteria σ^2_{i+} and σ^2_{j+} of Mode-2 operation are used only if $\mathrm{sgn}(i^*_{C,i}) = 1$ and $\mathrm{sgn}(i^*_{C,j}) = 1$, respectively. For example, in Sector II, while $\mathrm{sgn}(i^*_{C,i}) = 1$ and $\mathrm{sgn}(i^*_{C,j}) = 1$, σ^2_{i+} and σ^2_{j+} of Mode-2 operation are used to dictate the switching states of legs a and c. Thus, $\vec{U}_5$ is chosen if $\mathrm{sgn}(\sigma^2_{i+}) = 1$ and $\mathrm{sgn}(\sigma^2_{j+}) = 0$.

In Table II, vectors printed in boldface represent the adjacent active vectors to replace the null vectors. Two optional adjacent active vectors in the table, such as $\vec{U}_{1/4}$ in Sector II, mean that either $\vec{U}_1$ or $\vec{U}_4$ can be chosen based on the vector at the last sampling instant. For example, if previous vector is $\vec{U}_1$, the corresponding adjacent active vector to replace the null vector is chosen as $\vec{U}_1$. Similarly, $\vec{U}_4$ is chosen if the previous vector is $\vec{U}_4$. Either $\vec{U}_1$ or $\vec{U}_4$ can be selected if the previous vector is $\vec{U}_5$. Such choosing criterion eliminates null vectors on the premise of near constant switching frequency.

IV. Parametric Sensitivities

The BC2 switching criteria formulated in Section III are based on assuming that the filter parameters are the same and equal their nominal values. However, due to the manufacturing tolerance, temperature, and aging effect, the filter parameters will vary and drift. Thus, the system performance under filter parameter and grid impedance variations should be investigated.

Take $i = AB$ as an example. Let $\alpha_k \in (-0.2, +0.2), \beta_k \in (-0.1, +0.1)$, and $\gamma_k \in (-0.2, +0.2)$, $(k = a, b,$ or $c)$ be the tolerances of the inverter-side filter inductor $L_{1,k}$, filter capacitor $C_{f,k}$, and grid-side filter inductor $L_{2,k}$, respectively. Thus, $L_{1,k} = (1+\alpha_k)L_{1,N}, C_{f,k} = (1+\beta_k)C_{f,N}$, and $L_{2,k} = (1+\gamma_k)L_{2,N}$. $L_{1,N}, C_{f,N}$, and $L_{2,N}$ are the nominal values of $L_{1,k}, C_{f,k}$, and $L_{2,k}$, respectively.

The transfer functions of the proposed controller, including the BC2 and the intracycle information recovery mechanism as introduced in Section III, are expressed as (i.e., $i = \mathrm{AB}$)

$$\Delta U^*_{C,\mathrm{AB}}(s) - \Delta U_{g,\mathrm{AB}}(s) + \frac{T_{SW}}{4(1+\alpha_b)C_{f,N}}\{[\Delta I_{1,\mathrm{AB}}(s) - \Delta I_{g,\mathrm{ref,AB}}(s)] + G_R(s)[\Delta I_{g,\mathrm{AB}}(s) - \Delta I_{g,\mathrm{ref,AB}}(s)]\} = 0 \tag{11a}$$

$$\Delta U^*_{C,\mathrm{AB}}(s) = \frac{1}{sT_{\mathrm{in}}+1}\Delta U_{C,\mathrm{AB}}(s) + \frac{T_{\mathrm{in}}}{(sT_{\mathrm{in}}+1)C_{f,N}} \times \left\{ \begin{array}{c} \Delta I_{1,\mathrm{AB}}(s) - \Delta I_{g,\mathrm{ref,AB}}(s) \\ + G_R(s)[\Delta I_{g,\mathrm{AB}}(s) - \Delta I_{g,\mathrm{ref,AB}}(s)] \end{array} \right\}. \tag{11b}$$

Detailed derivations of (11) are given in Appendix B.

$\Delta I_{1,\mathrm{AB}}(s), \Delta U_{C,\mathrm{AB}}(s)$, and $\Delta U_{g,\mathrm{AB}}(s)$ in (11) can be derived, by considering the state-space equations in (1) and (2)

TABLE II
SWITCHING TABLE FOR THE CURRENT-MODE BC2 WITH NULL VECTORS EXCLUDED

sgn						I	II	III	IV	V	VI
$\left(\mathrm{i}^*_{C,i}\right)$	$\left(\mathrm{i}^*_{C,j}\right)$	$\left(\sigma^2_{i+}\right)$	$\left(\sigma^2_{i-}\right)$	$\left(\sigma^2_{j+}\right)$	$\left(\sigma^2_{j-}\right)$	$\begin{pmatrix} i=\mathrm{BC} \\ j=\mathrm{CA} \end{pmatrix}$	$\begin{pmatrix} i=\mathrm{AB} \\ j=\mathrm{BC} \end{pmatrix}$	$\begin{pmatrix} i=\mathrm{CA} \\ j=\mathrm{AB} \end{pmatrix}$	$\begin{pmatrix} i=\mathrm{BC} \\ j=\mathrm{CA} \end{pmatrix}$	$\begin{pmatrix} i=\mathrm{AB} \\ j=\mathrm{BC} \end{pmatrix}$	$\begin{pmatrix} i=\mathrm{CA} \\ j=\mathrm{AB} \end{pmatrix}$
1	1	0	/	0	/	$\vec{U}_5$	$\vec{U}_1$	$\vec{U}_6$	$\vec{U}_4$	$\vec{U}_3$	$\vec{U}_2$
				1		$\vec{U}_1$	$\vec{\boldsymbol{U}}_{\boldsymbol{4}}$	$\vec{\boldsymbol{U}}_{\boldsymbol{5}}$	$\vec{\boldsymbol{U}}_{\boldsymbol{2}}$	$\vec{U}_2$	$\vec{U}_3$
		1		0		$\vec{\boldsymbol{U}}_{\boldsymbol{3}}$	$\vec{U}_5$	$\vec{U}_4$	$\vec{U}_6$	$\vec{\boldsymbol{U}}_{\boldsymbol{6}}$	$\vec{\boldsymbol{U}}_{\boldsymbol{1}}$
				1		$\vec{U}_3$	$\vec{U}_4$	$\vec{U}_5$	$\vec{U}_2$	$\vec{U}_6$	$\vec{U}_1$
	0	0		/	0	$\vec{U}_1$	$\vec{\boldsymbol{U}}_{\boldsymbol{1/4}}$	$\vec{\boldsymbol{U}}_{\boldsymbol{5/6}}$	$\vec{\boldsymbol{U}}_{\boldsymbol{2/4}}$	$\vec{U}_2$	$\vec{U}_3$
					1	$\vec{U}_5$	$\vec{U}_1$	$\vec{U}_6$	$\vec{U}_4$	$\vec{U}_3$	$\vec{U}_2$
		1			0	$\vec{U}_3$	$\vec{U}_4$	$\vec{U}_5$	$\vec{U}_2$	$\vec{U}_6$	$\vec{U}_1$
					1	$\vec{\boldsymbol{U}}_{\boldsymbol{3/5}}$	$\vec{U}_5$	$\vec{U}_4$	$\vec{U}_6$	$\vec{\boldsymbol{U}}_{\boldsymbol{3/6}}$	$\vec{\boldsymbol{U}}_{\boldsymbol{1/2}}$
0	1	/	0	0	/	$\vec{\boldsymbol{U}}_{\boldsymbol{3/5}}$	$\vec{U}_5$	$\vec{U}_4$	$\vec{U}_6$	$\vec{\boldsymbol{U}}_{\boldsymbol{3/6}}$	$\vec{\boldsymbol{U}}_{\boldsymbol{1/2}}$
				1		$\vec{U}_3$	$\vec{U}_4$	$\vec{U}_5$	$\vec{U}_2$	$\vec{U}_6$	$\vec{U}_1$
			1	0		$\vec{U}_5$	$\vec{U}_1$	$\vec{U}_6$	$\vec{U}_4$	$\vec{U}_3$	$\vec{U}_2$
				1		$\vec{U}_1$	$\vec{\boldsymbol{U}}_{\boldsymbol{1/4}}$	$\vec{\boldsymbol{U}}_{\boldsymbol{5/6}}$	$\vec{\boldsymbol{U}}_{\boldsymbol{2/4}}$	$\vec{U}_2$	$\vec{U}_3$
	0		0	/	0	$\vec{U}_3$	$\vec{U}_4$	$\vec{U}_5$	$\vec{U}_2$	$\vec{U}_6$	$\vec{U}_1$
					1	$\vec{\boldsymbol{U}}_{\boldsymbol{5}}$	$\vec{U}_5$	$\vec{U}_4$	$\vec{U}_6$	$\vec{\boldsymbol{U}}_{\boldsymbol{3}}$	$\vec{\boldsymbol{U}}_{\boldsymbol{2}}$
			1		0	$\vec{U}_1$	$\vec{\boldsymbol{U}}_{\boldsymbol{1}}$	$\vec{\boldsymbol{U}}_{\boldsymbol{6}}$	$\vec{\boldsymbol{U}}_{\boldsymbol{4}}$	$\vec{U}_2$	$\vec{U}_3$
					1	$\vec{U}_5$	$\vec{U}_1$	$\vec{U}_6$	$\vec{U}_4$	$\vec{U}_3$	$\vec{U}_2$

with the tolerances of filter parameters taken into account

$$\Delta I_{1,\mathrm{AB}}(s) = \begin{Bmatrix} \Delta I_{g,\mathrm{AB}}(s) + s^2[(L_{2,a}+L_g)C_{f,a}\Delta I_{g,A}(s) \\ -(L_{2,b}+L_g)C_{f,b}\Delta I_{g,B}(s)] + s[C_{f,a}\cdot \\ \Delta U'_{g,\mathrm{Ao}}(s) - C_{f,b}\cdot\Delta U'_{g,\mathrm{Bo}}(s)] \end{Bmatrix} \tag{12a}$$

$$\Delta U_{C,\mathrm{AB}}(s) = \Delta U'_{g,\mathrm{AB}}(s) + s(L_{2,a}+L_g)\Delta I_{g,A}(s) - s(L_{2,b}+L_g)\Delta I_{g,B}(s) \tag{12b}$$

$$\Delta U_{g,\mathrm{AB}}(s) = \Delta U'_{g,\mathrm{AB}}(s) + sL_g\Delta I_{g,\mathrm{AB}}(s). \tag{12c}$$

Thus, a multiple-input-multiple-output (MIMO) system, including $\Delta I_{g,\mathrm{AB}}(s), \Delta U'_{g,\mathrm{AB}}(s), \Delta I_{g,B}(s)$, and $\Delta U'_{g,\mathrm{Bo}}(s)$, is derived

$$\Delta I_{g,\mathrm{AB}}(s) = \begin{Bmatrix} G_{I,\mathrm{AB}}(s)\Delta I_{g,\mathrm{ref,AB}}(s) + G_{V,\mathrm{AB}}(s)\Delta U'_{g,\mathrm{AB}} \\ (s)+G_{I,B}(s)\Delta I_{g,B}(s)+G_{V,B}(s)\Delta U'_{g,\mathrm{Bo}}(s) \end{Bmatrix} \tag{13}$$

where $G_{I,AB}, G_{V,AB}, G_{I,B}$, and $G_{V,B}$ are given in (14a)–(14d) shown at the bottom of the page,

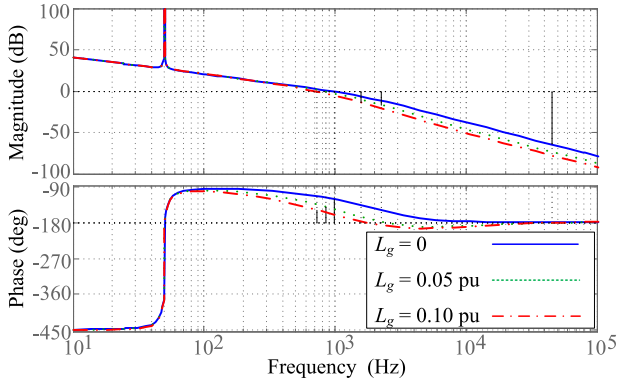

Fig. 8. Frequency plots of $G_{O,\mathrm{AB}}(s)$ with different grid inductances.

in which

$$b_1 = \frac{T_{SW}T_{\mathrm{in}}}{4(1+\alpha_b)},\quad b_0 = \left[\frac{T_{SW}}{4(1+\alpha_b)} + T_{\mathrm{in}}\right],$$

$$a_3 = \frac{T_{SW}T_{\mathrm{in}}(1+\lambda_g)(1+\gamma_a)(1+\beta_a)L_{2,N}C_{f,N}}{4(1+\alpha_b)},$$

$$a_2 \cong \left\{\frac{T_{\mathrm{SW}}(1+\lambda_g)(1+\beta_a)}{4(1+\alpha_b)} + T_{\mathrm{in}}[(1+\beta_a)+\beta_a\lambda_g]\right\} \times (1+\gamma_a)L_{2,N}C_{f,N}, a_1 = (1+\gamma_a)L_{2,N}C_{f,N},$$

and λ_g is the ratio between L_g and L_2.

$$G_{I,\mathrm{AB}}(s) = \frac{(sb_1+b_0)[1+G_R(s)]}{s^3a_3+s^2a_2+sa_1+(sb_1+b_0)[1+G_R(s)]} \tag{14a}$$

$$G_{V,\mathrm{AB}}(s) = -\frac{s[(sb_1+b_0)(1+\beta_a)-T_{\mathrm{in}}]C_{f,N}}{s^3a_3+s^2a_2+sa_1+(sb_1+b_0)[1+G_R(s)]} \tag{14b}$$

$$G_{I,B}(s) = -\frac{\{s^2(sb_1+b_0)[(1+\beta_a)(1+\gamma_a)-(1+\beta_b)(1+\gamma_b)]+s(\gamma_a-\gamma_b)\}(1+\lambda_g)L_{2,N}C_{f,N}}{s^3a_3+s^2a_2+sa_1+(sb_1+b_0)[1+G_R(s)]} \tag{14c}$$

$$G_{V,B}(s) = -\frac{s(sb_1+b_0)(\beta_a-\beta_b)C_{f,N}}{s^3a_3+s^2a_2+sa_1+(sb_1+b_0)[1+G_R(s)]} \tag{14d}$$

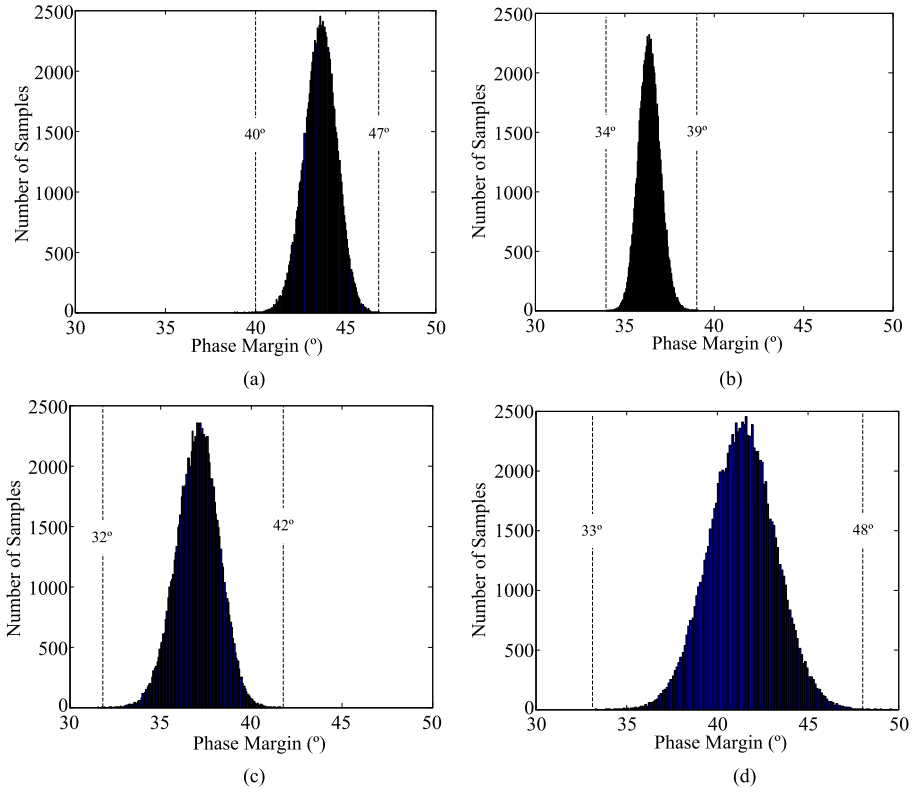

Fig. 9. Histogram distribution of the phase margin variation when $L_g = 0.1$ p.u. (a) $\alpha_k \in (-0.2, +0.2)$, $\beta_k = 0$, and $\gamma_k = 0$. (b) $\alpha_k = 0$, $\beta_k \in (-0.1, +0.1)$, and $\gamma_k = 0$. (c) $\alpha_k = 0$, $\beta_k = 0$, and $\gamma_k \in (-0.2, +0.2)$. (d) $\alpha_k \in (-0.2, +0.2)$, $\beta_k \in (-0.1, +0.1)$, and $\gamma_k \in (-0.2, +0.2)$.

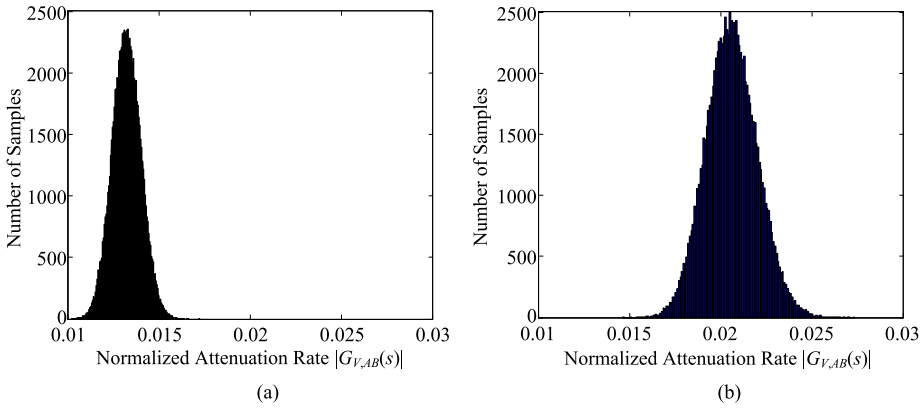

Fig. 10. Histogram distribution of the effect of harmonics in $u'_{g,\mathrm{AB}}$ on grid current $i_{g,\mathrm{AB}}$ when $L_g = 0.1$ p.u. (a) Effect of 5th harmonic component. (b) Effect of 7th harmonic component.

Under the balanced condition, i.e., $\alpha_a = \alpha_b, \beta_a = \beta_b$ and $\gamma_a = \gamma_b$, the grid current $i_{g,\mathrm{AB}}$ is only affected by the reference current command $i_{g,\mathrm{ref,AB}}$ and the corresponding grid voltage $u'_{g,\mathrm{AB}}$. The transfer function from $i_{g,\mathrm{ref,AB}}$ to $i_{g,\mathrm{AB}}, G_{I,\mathrm{AB}}(s)$, is the closed-loop gain of the control system, while the transfer function from $u'_{g,\mathrm{AB}}$ to $i_{g,\mathrm{AB}}, G_{V,\mathrm{AB}}(s)$, represents the disturbance attenuation of grid current against grid harmonic voltage. In the unbalanced condition, i.e., $\beta_a \neq \beta_b$ or $\gamma_a \neq \gamma_b$, two additional disturbances $i_{g,B}$ and $u'_{g,\mathrm{Bo}}$ from adjacent phase are brought in, since $G_{I,B}(s) \neq 0$ and $G_{V,B}(s) \neq 0$ as shown in (14c) and (14d). To distinguish them, $G_{I,\mathrm{AB}}(s)$ and $G_{V,\mathrm{AB}}(s)$ are named as functions with balanced filter parameters, while $G_{I,B}(s)$ and $G_{V,\mathrm{Bo}}(s)$ are named as corrected functions due to unbalanced filter parameters. Fig. 7 shows the relationship of such MIMO system with the consideration of the tolerances and possible unbalance of filter parameters, where $\Delta U'_{g,\mathrm{AB}}(s), \Delta I'_{g,B}(s)$, and $\Delta U'_{g,\mathrm{Bo}}(s)$ represent the disturbance sources.

Based on the equation $G_{I,\mathrm{AB}}(s)$, the open-loop gain from the error signal of the grid current $(\Delta I_{g,\mathrm{ref,AB}}(s) - \Delta I_{g,\mathrm{AB}}(s))$ to the grid current $\Delta I_{g,\mathrm{AB}}(s), G_{O,\mathrm{AB}}(s)$, is given

$$G_{O,\mathrm{AB}}(s) = \frac{(sb_1 + b_0)[1 + G_R(s)]}{s^3 a_3 + s^2 a_2 + s a_1} \tag{15}$$

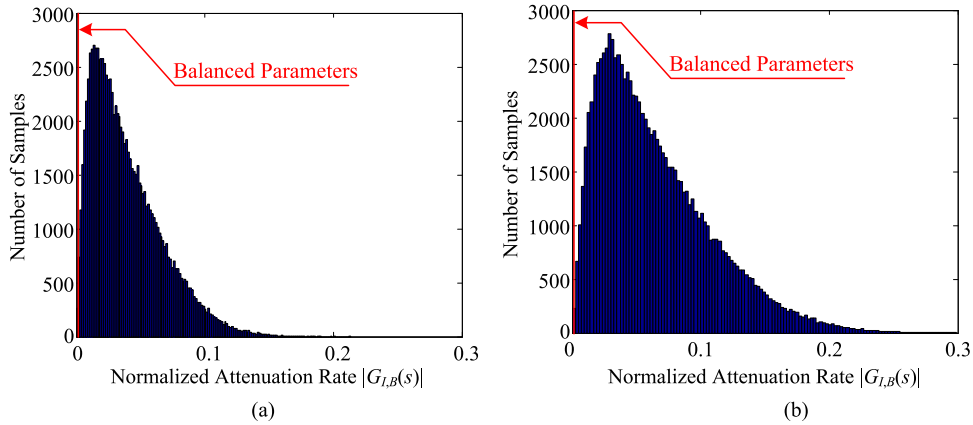

Fig. 11. Histogram distribution of the effect of harmonics in $i_{g,B}$ on grid current $i_{g,\mathrm{AB}}$ when $L_g = 0.1$ p.u. (a) Effect of 5th harmonic component. (b)Effect of 7th harmonic component.

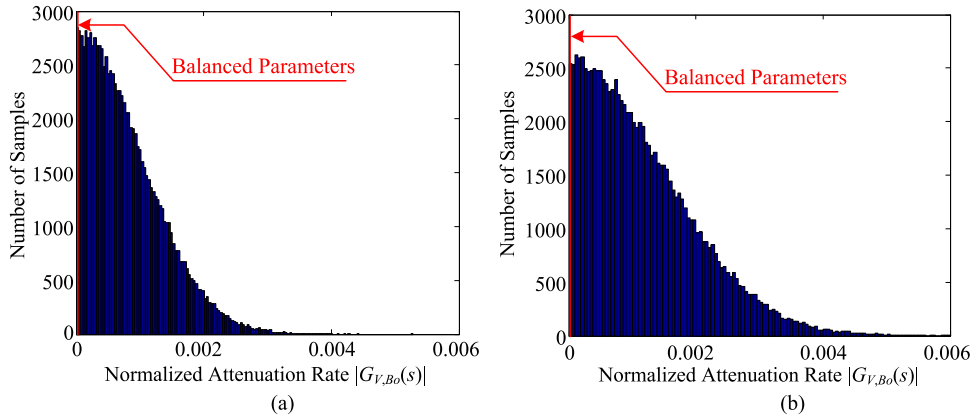

Fig. 12. Histogram distribution of the effect of harmonics in $u'_{g,\mathrm{Bo}}$ on grid current $i_{g,\mathrm{AB}}$ when $L_g = 0.1$ p.u. (a) Effect of 5th harmonic component. (b) Effect of 7th harmonic component.

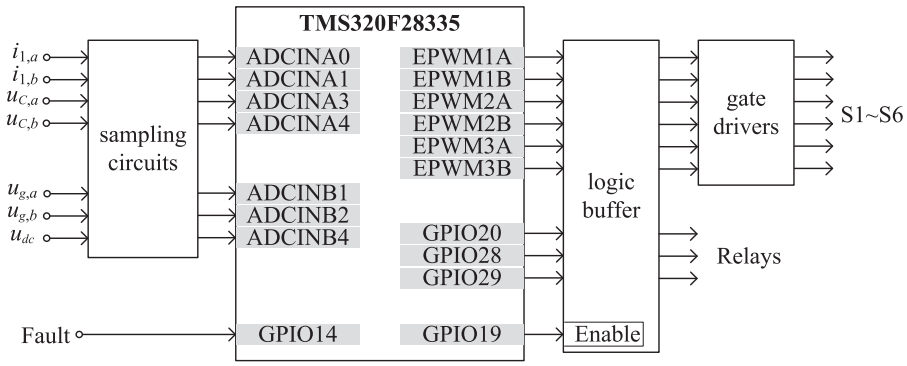

Fig. 13. Hardware implementation with the DSP.

According to the nominal parameters tabulated in Table III, the open-loop gain of the system under different values of L_g is shown in Fig. 8. The system performance under a wide variation of grid inductance with λ_g varying from 0 to 4.3 (430%) is studied. By using the capacitor current error (i.e., e_{AB}) feedforward given in (5a), the loop gain at the line frequency is enhanced much and thereby the error between the current command $i_{g,\mathrm{ref,AB}}$ and the grid current $i_{g,\mathrm{AB}}$ can be minimized under filter parametric variation. Moreover, as L_g increases from 0 ($\lambda_g = 0$) to 0.1 p.u. ($\lambda_g = 4.3$), the phase margin can still be maintained around 37°.

However, the tolerances and unbalance of the filter parameters would lead to the variation of the system performance practically. Based on (14), it is known that not only the functions under balanced filter parameters will be affected by the tolerances of filter parameters but also the corrected functions would be brought in and give impact on the injected current, as shown in Fig. 7. Thus, the parametric sensitivities of the

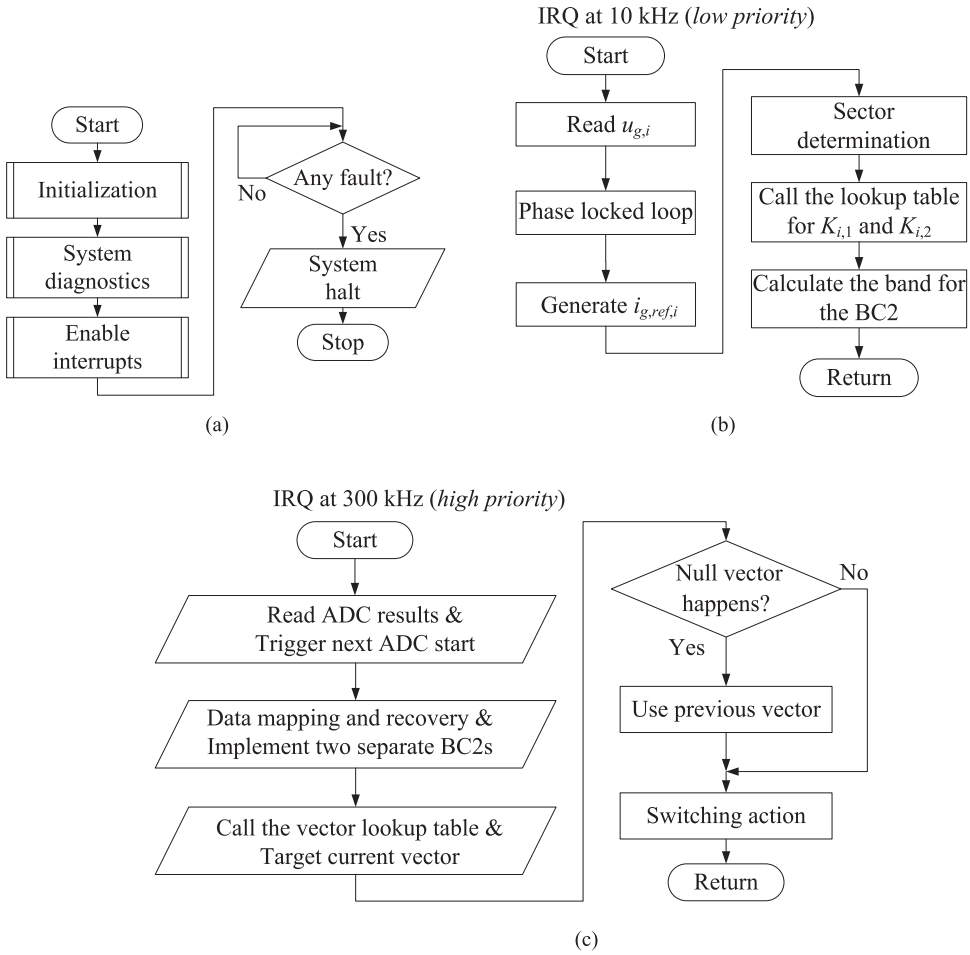

Fig. 14. Software flowchart in the DSP. (a) Main program, (b) low priority interrupt service routine, (c) high priority interrupt service routine.

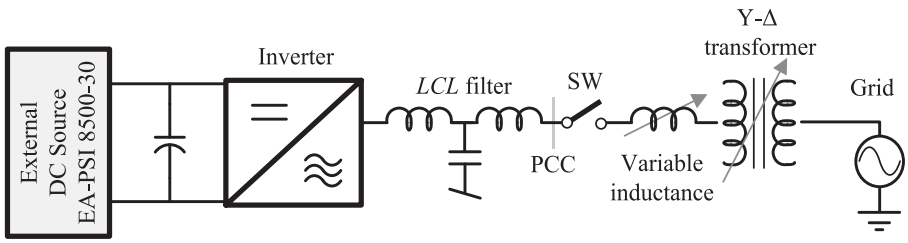

Fig. 15. Experimental setup with variable grid inductance.

TABLE III
VALUES OF THE COMPONENTS USED IN THE INVERTER PROTOTYPE

	LCL filter			Grid impedance	Switching frequency	Sampling frequency	DC bus voltage	Grid voltage	Rated power
System Parameter	L_1	L_2	C_f	L_g	f_{SW}	f_S	u_{in}	u_g'	P_{rated}
Value (pu*)	3.6 mH (0.07)	1.2 mH (0.023)	16 μF (0.08)	0.8~5.2 mH (0.016~0.10)	5 kHz	300 kHz	360 V	127 V	3000 W

*The base value for calculating the per unit (pu) is $3u_g^2 / P_{rated}$.

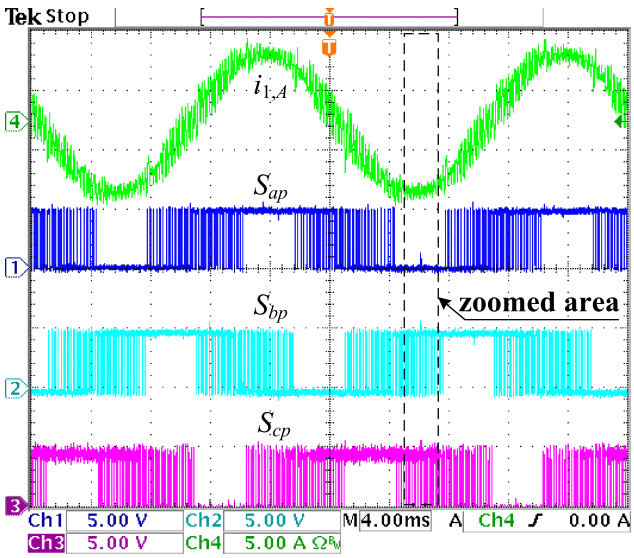

Fig. 16. Experimental waveforms with 60° DPWM.

system should be evaluated by analyzing the characteristics of both functions under balanced filter parameters and corrected functions. Assume that the tolerances of the filter parameters are all Gaussian distributed. A Monte-Carlo analysis is conducted on MATLAB to evaluate such parametric sensitivities to the system performance.

Fig. 9 shows the histogram distributions of the phase margin variation, due to manufacturing error and aging, which is valid because the phase margin is a critical factor to study the system stability based on Fig. 8. The horizontal axis represents the phase margin at the worst-case condition of $L_g = 0.10$ p.u. The vertical axis represents the number of samples with the considered tolerances of filter parameters. The total number of samples used in the simulation is 100 000. Fig. 9(a) shows the histogram generated for the case with $\alpha_k \in (-0.2, +0.2)$, $\beta_k = 0$, and $\gamma_k = 0$ ($k = a$ and b). Fig. 9(b) shows the histogram generated for the case with $\alpha_k = 0$, $\beta_k \in (-0.1, +0.1)$, and $\gamma_k = 0$. Fig. 9(c) shows the histogram generated for the case with $\alpha_k = 0$, $\beta_k = 0$, and $\gamma_k \in (-0.2, +0.2)$. Fig. 9(d) shows the histogram generated for the case with $\alpha_k \in (-0.2, +0.2)$, $\beta_k \in (-0.1, +0.1)$, and $\gamma_k \in (-0.2, +0.2)$. The phase margin is mainly affected by the tolerance of $L_{2,k}$ compared with that of $L_{1,k}$ and $C_{f,k}$. The maximum difference of the phase margin under the tolerance of $L_{2,k}$ is about 10°. Considering all tolerances of $L_{1,k}$, $L_{2,k}$, and $C_{f,k}$, the variation of the phase margin increases to 15°, which should be taken into account in the design procedure of the controller parameters.

Similarly, Fig. 10 shows the histogram distributions of the effect of the harmonic voltage in $u'_{g,\mathrm{AB}}$ on grid current $i_{g,\mathrm{AB}}$, where the effects of the major 5th and 7th harmonic voltage are studied. The horizontal axis represents the normalized attenuation rate $|G_{V,\mathrm{AB}}(s)|$ at the worst-case condition of $L_g = 0.10$ p.u. Considering the effect of filter parameters tolerances, most of the normalized attenuation rate of 5th and 7th harmonic voltage is lower than 1.5% (or 0.015) and 2.5% (or 0.025), respectively. For example, 5% distortion of 7th harmonic voltage would ideally lead to ∼1.2% grid current distortion for a 3 kW, 127 V, 50 Hz system, which is still maintained below the statutory limit, THDi < 5%.

Similar analysis is conducted in the evaluation of functions under unbalanced filter parameters. Figs. 11 and 12 show the histogram distributions of the effects of the harmonic current in $i_{g,B}$ and harmonic voltage in $u'_{g,\mathrm{Bo}}$ on $i_{g,\mathrm{AB}}$, respectively. Under balanced condition, there is no impact of $i_{g,B}$ and $u'_{g,\mathrm{Bo}}$ on $i_{g,\mathrm{AB}}$ since $G_{I,B}(s) = 0$ and $G_{V,B}(s) = 0$. Under unbalanced condition with considered parameters tolerances, the effect of $u'_{g,\mathrm{Bo}}$ on $i_{g,\mathrm{AB}}$ is minor and can be hence ignored, while the effect of harmonic current in $i_{g,B}$ is significant due to large harmonic attenuation rate. $i_{g,B}$ is tracked to the sinusoidal reference current $i_{g,B,\mathrm{ref}}$, which is included in $i_{g,AB,\mathrm{ref}}(i_{g,A,\mathrm{ref}} - i_{g,B,\mathrm{ref}})$ and $i_{g,BC,\mathrm{ref}}(i_{g,B,\mathrm{ref}} - i_{g,C,\mathrm{ref}})$. Thus, there are few harmonic components in $i_{g,B}$ reflecting on $i_{g,\mathrm{AB}}$.

Based on the above mathematical analysis, the proposed control scheme can guarantee system stability and maintain harmonic rejection capability of injected current even with significant tolerances and unbalance of filter parameters, and variable grid impedance.

V. Experimental Verifications

A 3 kW, 127 V, 50 Hz prototype has been built and evaluated for demonstration purpose. The design parameters are given in Table III. The filter parameters are chosen by adopting the design method given in [2]. The prototype is supplied by an external dc power supply EA-PSI 8500-30. The digital controller is Texas Instruments TMS320F28335. Fig. 13 shows the implementation on the DSP. The control flowchart is shown in Fig. 14. The control laws are implemented with two interrupt service routines, as depicted in Fig. 14(b) and (c). In the high priority routine, circuit variables are measured with the sampling frequency of 300 kHz. The sampling frequency of circuit variables for the boundary control method is higher than the switching frequency so as to keep tracking the state trajectories precisely [37], [44]. The experimental setup with variable grid inductance is presented in Fig. 15 and the inverter prototype is connected to a 380 V, 50 Hz power grid through a star-delta transformer. The following tests are studied.

A. Null Vector Excluded and Near Constant Frequency Operation

Fig. 16 shows the inverter output current waveform with 60° DPWM. Active bridges are controlled by the proposed current-mode BC2 based on the switching table in Table II. The switching states in Sector VI are zoomed in Fig. 17(a). The null vectors are avoided by using the proposed modulating scheme shown in Fig. 17(b). Moreover, the switching frequency is shown to be near constant by studying the period of every gate pulse shown in Fig. 17(a).

However, if one uses three separate BC2–DBC controllers by duplicating the methods in [41], the switching frequency is varied even with a regulated band, as shown in Fig. 18, due to the cross-coupled circuit variables amongst phases. Moreover, numerous current sensors are required.

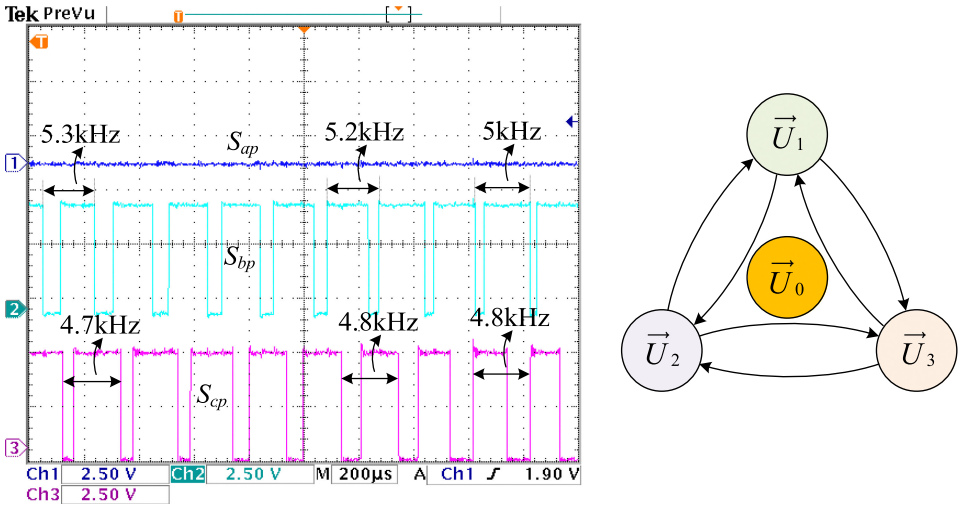

(a) (b)

Fig. 17. Voltage vectors with null vector excluded in Sector VI. (a) Zoomed switch states, (b) flow of voltage vectors.

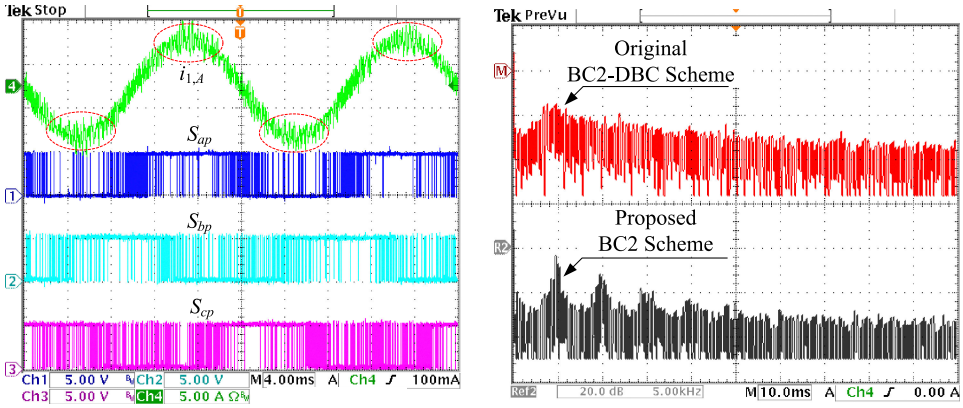

(a) (b)

Fig. 18. Comparison between original BC2-DBC scheme and proposed BC2 scheme. (a) Original BC2-DBC, (b) spectrum of gate pulses.

B. System Startup and Steady-State Waveforms

The startup performance is examined. Fig. 19 shows the system startup waveform of the injected current, where the phase of the terminal voltage $u_{g,\mathrm{Ao}}$ has been locked before system startup and thereby the PF of the injected current $i_{g,A}$ is ensured to be unity with the current-mode BC2 having filter capacitor current error feedforward. Fig. 20 shows the steady-state waveforms. According to the spectrum of the modulating waveform for S_{ap}, the switching frequency is maintained around 5 kHz owing to the decoupled modulating operation. The measured total-harmonic-distortion (THD) of the terminal voltage and the injected current are 1.9% and 1.8%, respectively.

C. Transient Performance

The transient performance of the inverter is investigated under different grid inductances, when the PF command is programmed to change from 1 to 0.707, and vice-versa. The corresponding experimental waveforms are shown in Fig. 21. It reveals that the response time of the proposed control is

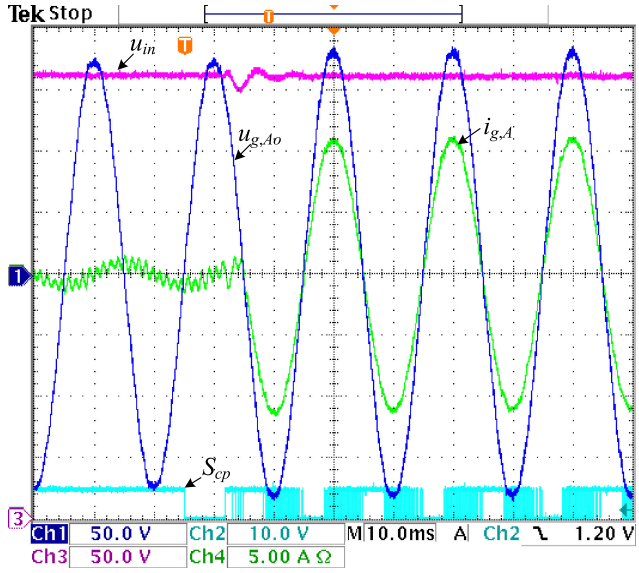

Fig. 19. Startup waveforms.

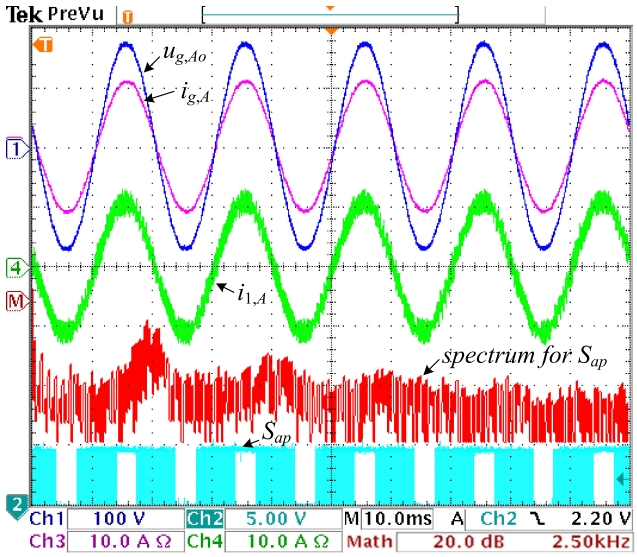

Fig. 20. Steady-state waveforms.

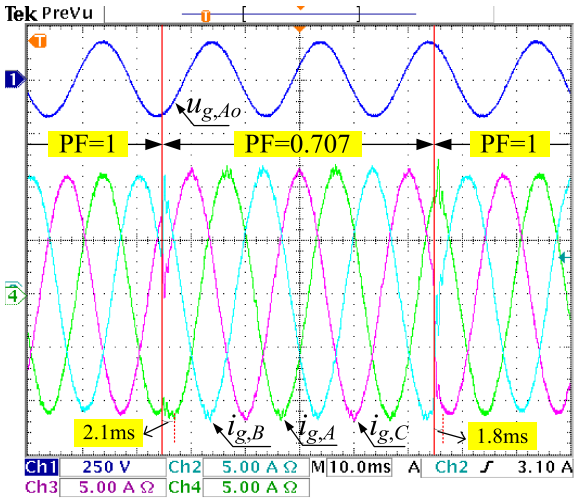

(a)

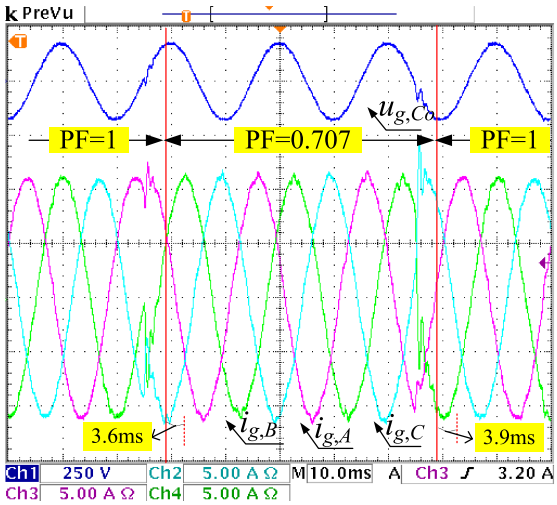

(b)

Fig. 21. Transient response under a sudden change of the PF command. (a) $L_g = 0.016$ p.u. (b) $L_g = 0.10$ p.u.

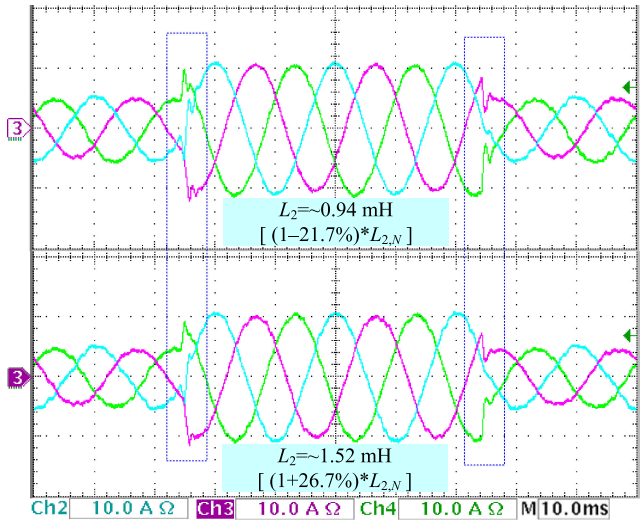

Fig. 22. Transient behaviors under different grid-side filter inductance drifting.

around 2 ms and 3.6 ms in the stiff and weak grid conditions, respectively, matching with the mathematical model in Section IV. The inverter operates well with reactive power injection (PF = 0.707) owing to the equivalence of the bidirectional dual-buck circuit based on Fig. 3(b). Since higher modulation index is needed at the condition of PF = 0.707, more steady-state current distortion is found both in the stiff and weak grid conditions with reactive power injection. For example, the THD of the injected current under the condition of PF = 1 and 0.707 in the weak grid increases from THDi = 2.0% at PF = 1 to THDi = 3.5% at PF = 0.707, which is still maintained below the statutory limit, THDi < 5%.

Based on the theoretical analysis of filter parametric sensitivities in Section IV, the tolerance of L_2 has impact on the phase margin. In Fig. 22, its effect on the system transient behaviors under the weak grid condition, i.e., $L_g = 0.10$ p.u., is studied. It is observed that the transient performance with large L_2 is slightly better than small L_2. It is because the phase margin increases much with larger L_2 as shown in Fig. 9(c). The core material of the grid-side inductor used in this test is Metglas@ AMCC from HITACHI [45], of which the permeability is relatively constant within the operating zone.

D. Harmonic Rejection Capability

To study the harmonic rejection capability of the system, a 1.5 kW six-pulse rectifier is shunted at the point-of-common-coupling (PCC) of a weak grid with $L_g = 0.10$ p.u. Fig. 23(a) shows the waveforms of $u_{g,\mathrm{Ao}}, i_{r,A}, i_{r,B}$, and $i_{r,C}$ (the input currents of the rectifier) with the inverter disabled. Serious oscillations appear at the terminal voltage and the input current of the rectifier. That is because the standby inverter output filter components, i.e., $L_{2,k}$ and $C_{f,k}$, are susceptible to the harmonics brought in by the six-pulse rectifier. Such oscillations are rejected effectively when the inverter is enabled as shown in Fig. 23(b). The reason is that the filter resonance has been attenuated in the transfer characteristics as shown in Fig. 8. Results

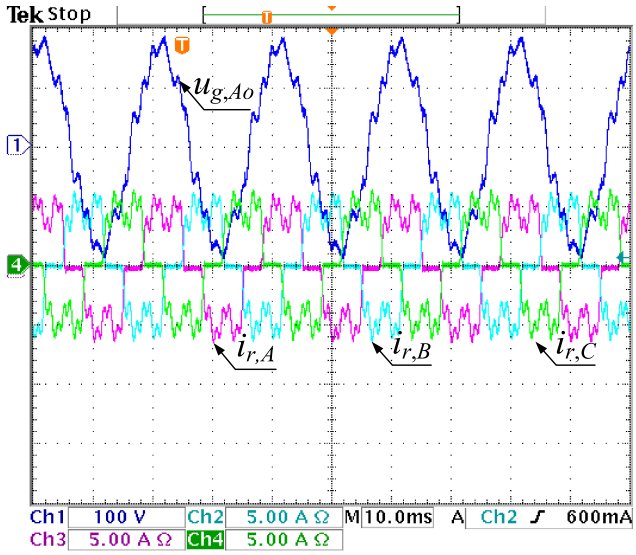

(a)

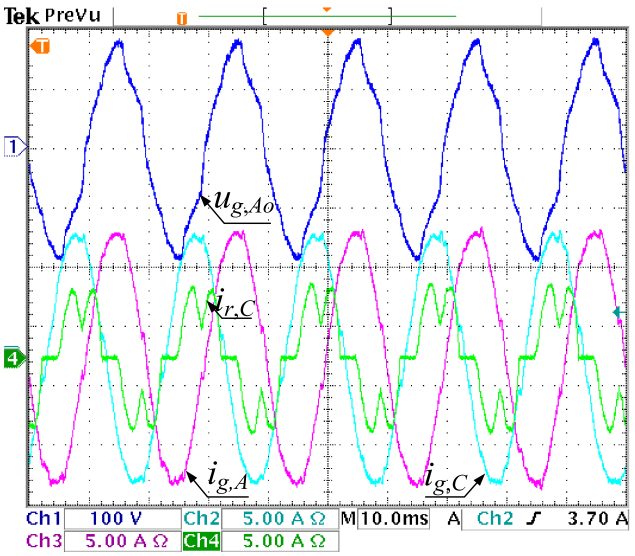

(b)

Fig. 23. Waveforms with a shunt six-pulse rectifier at the PCC. (a) With the inverter disabled. (b) With the inverter enabled.

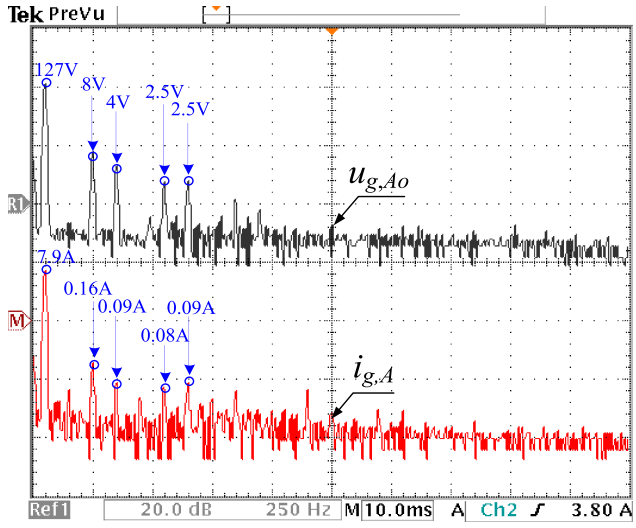

Fig. 24. Spectrums of the terminal voltage and injected current with six-pulse rectifier connected and $L_g = 0.10$ p.u.

in Fig. 24 reveal that the effect of rich low order harmonics at the terminal voltage on the injected current is also effectively rejected. For example, 6.4% and 3.2% harmonic voltage at 250 Hz and 350 Hz leads to 2.0% and 1.1% harmonic current, respectively, which matches with the theoretical analysis in Section IV. Thus, by using the proposed control scheme, the injected current (%THD = 3.9%) has much better quality than the terminal voltage (%THD = 8.4%) even with a shunt six-pulse rectifier at the PCC.

V. Conclusion

A BC2 controller that can directly track the output current of three-phase three-wire grid-connected inverter with reduced current sensing and fixed frequency operation has been proposed. The switching criteria are derived for current-mode operation without requiring extra current regulation control. Two separate sets of switching criteria are applied to a fictitious decoupled dual-buck structure with 60° DPWM, capacitor current error feedforward, and null vectors exclusion technique in the switching table.

Even with significant tolerances and unbalance of filter parameters, the proposed control system can still maintain high system stability and harmonic rejection capability under different grid conditions. Moreover, it allows feeding reactive power into the power grid, which would be favorable to the voltage support function of the inverter. The system steady-state, transient, and harmonic rejection performances under stiff and weak grids have been examined on a digitally-controlled 3 kW, 127 V, 50 Hz inverter prototype with an *LCL* filter.

Appendix

A. Derivations of (4)

When the switching intracycle information of circuit variables is considered, the state equations in (2) can be approximated as (i = AB, BC, or CA)

$$L_1 \frac{d}{dt} i_{C,i} = L_1 \frac{d}{dt}(i_{1,i} - i_{g,i})\Big|_{\frac{d}{dt} i_{g,i} \cong 0}$$

$$\cong L_1 \frac{d}{dt} i_{1,i} = u_{1,i} - u_{C,i} \tag{A1a}$$

$$i_{C,i} = C_f \frac{d}{dt} u_{C,i} \cong -C_f \frac{d}{dt}(u_{1,i} - u_{C,i})\Big|_{\frac{d}{dt} u_{1,i} \cong 0} \tag{A1b}$$

where the grid current $i_{g,i}$ is fairly constant over the switching period and the inverter output voltage $u_{1,i}$ in Mode-1 or Mode-2 is constant, which is $+u_{\text{in}}$ or 0, or $-u_{\text{in}}$. Thus, in terms of the switching surface, the derivatives of $i_{g,i}$ and $u_{1,i}$ are assumed to be zero.

By multiplying the above two equations and integrating both sides

$$L_1 \int i_{C,i} di_{C,i} \cong -C_f \int (u_{1,i} - u_{C,i}) d(u_{1,i} - u_{C,i}). \quad \text{(A2)}$$

By solving (A2) between t_1 and $t_1{}^+$ for one switching criterion (Mode-1) or t_2 and $t_2{}^+$ for another switching criterion (Mode-2) as shown in Fig. 5, it is obtained

$$\begin{aligned} L_1[i_{C,i}^2(t_1^+) - i_{C,i}^2(t_1)] = & -C_f\{[u_{1,i}(t_1^+) - u_{C,i}(t_1^+)]^2 \\ & - [u_{1,i}(t_1) - u_{C,i}(t_1)]^2\} \quad \text{(A3a)} \\ L_1[i_{C,i}^2(t_2^+) - i_{C,i}^2(t_2)] = & -C_f\{[u_{1,i}(t_2^+) - u_{C,i}(t_2^+)]^2 \\ & - [u_{1,i}(t_2) - u_{C,i}(t_2)]^2\}. \quad \text{(A3b)} \end{aligned}$$

To facilitate the BC2 operation, (A3) is further simplified in the following.

The time instants t_1^+ and t_2^+ are infinitesimally short after t_1 and t_2, respectively. Thus, based on Fig. 5, $u_{C,i}(t_1^+), u_{C,i}(t_2^+), i_{C,i}(t_1^+)$, and $i_{C,i}(t_2^+)$ are rewritten as

$$\begin{aligned} u_{C,i}(t_1^+) = & \; u_{C,i}(t_2^+) = u_{\mathrm{ref},i}(t) \quad \text{(A4a)} \\ i_{C,i}(t_1^+) = & \; i_{C,\mathrm{line},i}(t) - \Delta i_{C,i}(t) \quad \text{(A4b)} \\ i_{C,i}(t_2^+) = & \; i_{C,\mathrm{line},i}(t) + \Delta i_{C,i}(t). \quad \text{(A4c)} \end{aligned}$$

Because the variables at the time instant t_1 or t_2 keep being measured, t_1 and t_2 in (A3) can be replaced by t. Moreover, it has $u_{1,i}(t_1^+) = u_{1,i}(t_1)$ and $u_{1,i}(t_2^+) = u_{1,i}(t_2)$. Thus, by substituting (A4) into (A3), the following equations can be derived:

$$\begin{aligned} & L_1\{[i_{C,\mathrm{line},i}(t) - \Delta i_{C,i}(t)]^2 - i_{C,i}^2(t)\} \cong 2C_f[u_{1,i}(t) \\ & \quad - u_{C,i}(t)][u_{C,i}(t) - u_{\mathrm{ref},i}(t)] \quad \text{(A5a)} \\ & L_1\{[i_{C,\mathrm{line},i}(t) + \Delta i_{C,i}(t)]^2 - i_{C,i}^2(t)\} \cong 2C_f[u_{1,i}(t) \\ & \quad - u_{C,i}(t)][u_{C,i}(t) - u_{\mathrm{ref},i}(t)]. \quad \text{(A5b)} \end{aligned}$$

As tabulated in Table II, the information $(u_{1,i} - u_{C,i})$ in (A5) is different in Mode-1 and Mode-2 operation specific to a half-bridge and sector. Thus, the voltage-mode BC2 switching criteria of (4) are derived by rewriting (A5).

B. Derivations of (11)

As derived in [41], in fixed switching frequency operation, the small-signal models for Modes 1 and 2 in the current-mode BC2 [(10)] are obtained (i.e., $i = AB$ in Sector II)

$$\begin{aligned} \Delta u_{C,\mathrm{AB}}^*(t) \approx & \; \Delta u_{g,\mathrm{AB}}(t) - \frac{D_{\mathrm{AB}} T_{SW}}{2(1+\alpha_b)C_{f,N}}[\Delta i_{1,\mathrm{AB}}(t) \\ & - \Delta i_{g,\mathrm{ref,AB}}(t) + \Delta e_{\mathrm{AB}}(t)] \quad \text{(A6a)} \\ \Delta u_{C,\mathrm{AB}}^*(t) \approx & \; \Delta u_{g,\mathrm{AB}}(t) - \frac{(1-D_{\mathrm{AB}}) T_{SW}}{2(1+\alpha_b)C_{f,N}}[\Delta i_{1,\mathrm{AB}}(t) \\ & - \Delta i_{g,\mathrm{ref,AB}}(t) + \Delta e_{\mathrm{AB}}(t)] \quad \text{(A6b)} \end{aligned}$$

where $D_{\mathrm{AB}} = (t_2 - t_1)/T_{SW}$ is the duty ratio of Mode-1 in Fig. 5.

By adding (A6a) and (A6b) at both sides

$$\begin{aligned} \Delta u_{C,\mathrm{AB}}^*(t) = & \; \Delta u_{g,\mathrm{AB}}(t) - \frac{T_{SW}}{4(1+\alpha_b)C_{f,N}}[\Delta i_{1,\mathrm{AB}}(t) \\ & - \Delta i_{g,\mathrm{ref,AB}}(t) + \Delta e_{\mathrm{AB}}(t)] \quad \text{(A7)} \end{aligned}$$

where Δe_{AB} can be written as

$$\begin{aligned} \Delta e_{\mathrm{AB}}(t) = & \; \mathrm{BPF}_0[\Delta i_{1,\mathrm{AB}}(t) - \Delta i_{g,\mathrm{ref,AB}}(t) + \Delta e_{\mathrm{AB}}(t)] \\ & - C_{f,N} \frac{d}{dt}\{\mathrm{BPF}_0[\Delta u_{C,\mathrm{AB}}(t)]\} \\ \cong & \; \mathrm{BPF}_0[\Delta i_{g,\mathrm{AB}}(t) - \Delta i_{g,\mathrm{ref,AB}}(t)] \\ & + \mathrm{BPF}_0[\Delta e_{\mathrm{AB}}(t)] \quad \text{(A8)} \end{aligned}$$

in which BPF_0 means a band-pass filter for extracting the line-frequency component.

Transform (A7) and (A8) into s-domain and integrate them. Thus

$$\begin{aligned} & \Delta U_{C,\mathrm{AB}}^*(s) - \Delta U_{g,\mathrm{AB}}(s) + \frac{T_{SW}}{4(1+\alpha_b)C_{f,N}} \\ & \quad \times \{[\Delta I_{1,\mathrm{AB}}(s) - \Delta I_{g,\mathrm{ref,AB}}(s)] + \frac{G_{\mathrm{BPF}_0}(s)}{1 - G_{\mathrm{BPF}_0}(s)} \\ & \quad \times [\Delta I_{g,\mathrm{AB}}(s) - \Delta I_{g,\mathrm{ref,AB}}(s)]\} = 0 \quad \text{(A9)} \end{aligned}$$

where $G_{\mathrm{BPF}_0}(s)$ is the transfer function of the band-pass filter.

Simplify (A9) by using $G_R(s) = \frac{G_{\mathrm{BPF}_0}(s)}{1 - G_{\mathrm{BPF}_0}(s)}$, the transfer function of the current-mode BC2 in (11a) is derived. The HPF in Fig. 6 is ignored in the model as it has a narrow bandwidth (lower than 50 Hz) that does not affect the system stability and can simplify the analysis. Then, the following equations are obtained (i.e., $i = AB$ in Sector II)

$$sC_{f,N} \cdot \Delta U_{C,\mathrm{HF,AB}}(s) = \Delta I_{1,\mathrm{AB}}(s) - \Delta I_{g,\mathrm{ref,AB}}^*(s) \quad \text{(A10)}$$

$$sT_{\mathrm{in}} \cdot \Delta U_{C,\mathrm{LF,AB}}(s) = \Delta U_{C,\mathrm{AB}}(s) - \Delta U_{C,\mathrm{AB}}^*(s) \quad \text{(A11)}$$

$$\Delta U_{C,\mathrm{AB}}^*((s) = \Delta U_{C,\mathrm{HF,AB}}(s) + \Delta U_{C,\mathrm{LF,AB}}(s) \quad \text{(A12)}$$

By using (A10)–(A12), the transfer function of the intracycle information recovery mechanism in (11b) is derived.

REFERENCES

[1] M. Liserre, R. Teodorescu, and F. Blaabjerg, "Stability of photovoltaic and wind turbine grid-connected inverters for a large set of grid impedance values," *IEEE Trans. Power Electron.*, vol. 21, no. 1, pp. 263–272, Jan. 2006.

[2] W. Wu, Y. He, T. Tang, and F. Blaabjerg, "A new design method for the passive damped LCL and LLCL filter-based single-phase grid-tied inverter," *IEEE Trans. Ind. Electron.*, vol. 60, no. 10, pp. 4339–4350, Oct. 2013.

[3] R. N. Beres, X. Wang, F. Blaabjerg, M. Liserre, and C. L. Bak, "Optimal design of high-order passive-damped filters for grid-connected applications," *IEEE Trans. Power Electron.*, vol. 31, no. 3, pp. 2083–2098, Mar. 2015.

[4] R. Peña-Alzola, M. Liserre, F. Blaabjerg, R. Sebastián, J. Dannehl, and F. W. Fuchs, "Analysis of the passive damping losses in LCL-filter-based grid converters," *IEEE Trans. Power Electron.*, vol. 28, no. 6, pp. 2642–2646, Jun. 2013.

[5] V. Blasko and V. Kaura, "A novel control to actively damp resonance in input LC filter of a three-phase voltage source converter," *IEEE Trans. Ind. Appl.*, vol. 33, no. 2, pp. 542–550, Mar./Apr. 1997.

[6] M. Huang, X. Wang, P. C. Loh, and F. Blaabjerg, "Active damping of LLCL-filter resonance based on LC-trap voltage or current feedback," *IEEE Trans. Power Electron.*, vol. 31, no. 3, pp. 2337–2346, Mar. 2016.

[7] M. Hanif, V. Khadkikar, W. Xiao, and J. Kirtley, "Two degrees of freedom active damping technique for LCL filter-based grid connected PV systems," *IEEE Trans. Ind. Electron.*, vol. 61, no. 6, pp. 2795–2803, Jun. 2014.

[8] S. Parker, B. McGrath, and D. Holmes, "Regions of active damping control for LCL filters," *IEEE Trans. Ind. Appl.*, vol. 50, no. 1, pp. 424–432, Jan./Feb. 2014.

[9] M. Malinowski and S. Bernet, "A simple voltage sensorless active damping scheme for three-phase PWM converters with an LCL filter," *IEEE Trans. Ind. Electron.*, vol. 55, no. 4, pp. 1876–1880, Apr. 2008.

[10] J. Dannehl, C. Wessels, and F. W. Fuchs, "Limitations of voltage-oriented PI current control of grid-connected PWM rectifiers with LCL filters," *IEEE Trans. Ind. Electron.*, vol. 56, no. 2, pp. 380–388, Feb. 2009.

[11] R. Teodorescu, M. Liserre, and P. Rodríguez, *Grid Converters for Photovoltaic and Wind Power Systems*. Hoboken, NJ, USA: Wiley, 2011.

[12] Y. Liu, W. Wu, Y. He, Z. lin, F. Blaabjerg, and H. Chung, "An efficient and robust hybrid damper for LCL- or LLCL-based grid-tied inverter with strong grid-side harmonic voltage effect rejection," *IEEE Trans. Ind. Electron.*, vol. 63, no. 2, pp. 926–936, Feb. 2016.

[13] D. Pan, X. Ruan, C. Bao, W. Li, and X. Wang, "Capacitor-current-feedback active damping with reduced computation delay for improving robustness of LCL-type grid-connected inverter," *IEEE Trans. Power Electron.*, vol. 29, no. 7, pp. 3414–3427, Jul. 2014.

[14] X. Wang, Y. Pang, P. Loh, and F. Blaabjerg, "A series-LC-filtered active damper with grid disturbance rejection for AC power-electronics-based power systems," *IEEE Trans. Power Electron.*, vol. 30, no. 8, pp. 4037–4041, Aug. 2015.

[15] J. Sun, "Impedance-based stability criterion for grid-connected inverters," *IEEE Trans. Power Electron.*, vol. 26, no. 11, pp. 3075–3078, Nov. 2011.

[16] Y. Jia, J. Zhao, and X. Fu, "Direct grid current control of LCL-filtered grid-connected inverter mitigating grid voltage disturbance," *IEEE Trans. Power Electron.*, vol. 29, no. 3, pp. 1532–1541, Mar. 2014.

[17] J. He, Y. Li, and M. S. Munir, "A flexible harmonic control approach through voltage-controlled DG–grid interfacing converters," *IEEE Trans. Power Electron.*, vol. 59, no. 1, pp. 444–455, Jan. 2011.

[18] R. Teodorescu, F. Blaabjerg, M. Liserre, and P. C. Loh, "Proportional-resonant controllers and filters for grid-connected voltage-source converters," *IEE Proc.-Electr. Power Appl.*, vol. 153, no. 5, pp. 750–762, Sep. 2006.

[19] M. Liserre, F. Blaabjerg, and R. Teodorescu, "Grid impedance estimation via excitation of LCL-filter resonance," *IEEE Trans. Ind. Appl.*, vol. 43, no. 5, pp. 1401–1407, Sep./Oct. 2007.

[20] N. Hoffmann and F. W. Fuchs, "Minimal invasive equivalent grid impedance estimation in inductive–resistive power networks using extended Kalman filter," *IEEE Trans. Power Electron.*, vol. 29, no. 2, pp. 631–641, Apr. 2013.

[21] J. A. Suul, K. Ljøkelsøy, T. Midtsund, and T. Undeland, "Synchronous reference frame hysteresis current control for grid converter applications," *IEEE Trans. Ind. Appl.*, vol. 47, no. 5, pp. 2183–2194, Sep./Oct. 2011.

[22] L. A. Serpa, S. D. Round, and J. W. Kolar, "A virtual-flux decoupling hysteresis current controller for mains connected inverter systems," *IEEE Trans. Power Electron.* vol. 22, no. 5, pp. 1766–1777, Sep. 2007.

[23] M. A. Elsaharty, M. S. Hamad, and H. A. Ashour, "Digital hysteresis current control for grid-connected converters with LCL filter," in *Proc. 37th Annu. Conf. IEEE Ind. Electron. Soc.*, Nov. 2011, pp. 4685–4690.

[24] S. Cobreces, E. Bueno, F. J. Rodriguez, F. Huerta, and P. Rodriguez, "Influence analysis of the effects of an inductive-resistive weak grid over L and LCL filter current hysteresis controllers," in *Proc. Eur. Conf. Power Electron. Appl.* , Sep. 2007, pp. 1–10.

[25] T. Noguchi, H. Tomiki, S. Kondo, and I. Takahashi, "Direct power control of PWM converter without power-source voltage sensors," *IEEE Trans. Ind. Appl.*, vol. 34, no. 3, pp. 473–479, May/Jun. 1998.

[26] L. A. Serpa, S. Ponnaluri, P. M. Barbosa, and J. W. Kolar, "A modified direct power control strategy allowing the connection of three-phase inverters through LCL filters," *IEEE Trans. Ind. Appl.*, vol. 43, no. 5, pp. 1388–1400, Sep./Oct. 2007.

[27] J. Scoltock, T. Geyer, and U. Madawala, "Model predictive direct power control for a grid-connected converter with an LCL-filter," in *Proc. IEEE Int. Conf. Ind. Technol.*, Feb. 2013, pp. 588–593.

[28] J. Reese, R. Lohde, and F. W. Fuchs, "FRT capability of direct power controlled converters connected by an actively damped LCL-filter for wind power applications," in *Proc. 2011-14th Eur. Conf., Power Electron. Appl.*, Aug./Sep. 2011, pp. 1–10.

[29] H. Komurcugil, S. Ozdemir, I. Sefa, N. Altin, and O. Kukrer, "Sliding-mode control for single-phase grid-connected LCL-filtered VSI with double-band hysteresis scheme," *IEEE Trans. Ind. Electron.*, vol. 63, no. 2, pp. 864–873, Feb. 2016.

[30] F. Fuchs, J. Dannehl, and F. W. Fuchs, "Discrete sliding mode current control of grid-connected three-phase PWM converters with LCL filter," in *Proc. IEEE Int. Symp. Ind. Electron.*, Jul. 2010, pp. 779–785.

[31] X. Hao, X. Yang, T. Liu, L. Huang, and W. Chen, "A sliding-mode controller with multiresonant sliding surface for single-phase grid-connected VSI with an LCL filter," *IEEE Trans. Power Electron.*, vol. 28, no. 5, pp. 2259–2268, May 2013.

[32] O. Kukrer, H. Komurcugil, and A. Doganalp, "A three-level hysteresis function approach to the sliding-mode control of single-phase UPS inverters," *IEEE Trans. Ind. Electron.*, vol. 56, no. 9, pp. 3477–3486, Sep. 2009.

[33] K. Leung and H. Chung, "Derivation of a second-order switching surface in the boundary control of buck converters," *IEEE Power Electron. Lett.*, vol. 2, no. 2, pp. 63–67, Jun. 2004.

[34] J. Chiu, K. Leung, and H. Chung, "High-order switching surface in boundary control of inverters," *IEEE Trans. Power Electron.*, vol. 22, no. 5, pp. 1753–1765, May 2007.

[35] M. Ordonez, M. T. Iqbal, and J. E. Quaicoe, "Selection of a curved switching surface for buck converters," *IEEE Trans. Power Electron.*, vol. 21, no. 4, pp. 1148–1153, Jul. 2006.

[36] K. Leung and H. Chung, "A comparative study of the boundary control of buck converters using first- and second-order switching surfaces," *IEEE Trans. Power Electron.*, vol. 22, no. 4, pp. 1196–1209, Jul. 2007.

[37] M. Ordonez, J. E. Quaicoe, and M. T. Iqbal, "Advanced boundary control of inverters using the natural switching surface: Normalized geometrical derivation," *IEEE Trans. Power Electron.*, vol. 23, no. 6, pp. 2915–2930, Nov. 2008.

[38] R. Chan, H. Chung, and R. Hui, "A generalized theory of boundary control for a single-phase multilevel inverter using second-order switching surface," *IEEE Trans. Power Electron.* vol. 24, no. 10, pp. 2298–2313, Oct. 2009.

[39] J. M. Galvez and M. Ordonez, "Introducing the natural switching surface for reference frame systems: Three-phase boost PFCs," in *Proc. IEEE Energy Convers. Congr. Expo.*, 2012, pp. 1064–1070.

[40] J. Ge, Z. Zhao, L. Yuan, T. Lu, and F. He, "Direct power control based on natural switching surface for three-phase PWM rectifiers," *IEEE Trans. Power Electron.*, vol. 30, no. 6, pp. 2918–2922, Jun. 2015.

[41] Y. He, H. Chung, C. Ho, and W. Wu, "Use of boundary control with second-order switching surface to reduce the system order for deadbeat controller in grid-connected inverter," *IEEE Trans. Power Electron.*, vol. 31, no. 3, pp. 2638–2653, Mar. 2016.

[42] D. G. Holmes and T. A. Lipo, *Pulse Width Modulation for Power Converters*. Hoboken, NJ, USA: Wiley, 2003.

[43] C.-C. Hou, C.-C. Shih, P.-T. Cheng, and A. M. Hava, "Common-mode voltage reduction pulsewidth modulation techniques for three-phase grid-connected converters," *IEEE Trans. Power Electron.*, vol. 28, no. 4, pp. 1971–1979, Apr. 2013.

[44] L. Corradini, E. Orietti, P. Mattavelli, and S. Saggini, "Digital hysteretic voltage-mode control for DC–DC converters based on asynchronous sampling," *IEEE Trans. Power Electron.*, vol. 24, no. 1, pp. 201–211, Jan. 2009.

[45] Hitachi Metals Ltd., *Tokyo, Japan, Metglas@ AMCC Series Cut Core FINEMET@ 787 F3CC Series Cut Core*. Hitachi Metals Ltd. Apr. 2016. [Online]. Available: http://www.hitachi-metals.co.jp/products/elec/tel/pdf/hj-b11.pdf

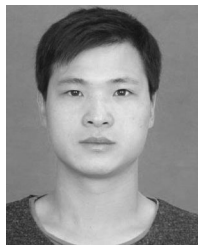

Yuanbin He (S'14) received the B.Eng. and M.Eng. degrees in electrical engineering from Shanghai Maritime University, Shanghai, China, in 2009 and 2011, respectively. He is currently working toward the Ph.D. degree in power electronics at City University of Hong Kong, Kowloon, Hong Kong.

He worked as an Associate Researcher with Nanjing FSP-Powerland Technology Inc., Nanjing, China until March 2013, where he engaged in research and development of dc–dc and dc–ac converters. From April to August 2013, he was a Research Assistant with the Centre for Smart Energy Conversion and Utilization Research, City University of Hong Kong, Kowloon, Hong Kong. From February to June 2016, he was a Visiting Scholar at the Department of Electrical and Computer Engineering, University of Manitoba, Canada. His current research interests include advanced digital control technologies for renewable energy generation system.

Henry Shu-hung Chung (M'95–SM'03–F'16) received the B.Eng. and Ph.D. degrees in electrical engineering from The Hong Kong Polytechnic University, Hong Kong, in 1991 and 1994, respectively.

Since 1995 he has been with the City University of Hong Kong. He is currently a Professor of the Department of Electronic Engineering and the Director of the Centre for Smart Energy Conversion and Utilization Research. His research interests include renewable energy conversion technologies, lighting technologies, smart grid technologies, and computational intelligence for power electronic systems. He has edited one book, authored eight research book chapters, more than 350 technical papers including 170 refereed journal papers in his research areas, and holds 35 patents.

Dr. Chung was Chair of the Technical Committee of the High-Performance and Emerging Technologies, IEEE Power Electronics Society in 2010–2014. He is currently Editor-in Chief of the IEEE POWER ELECTRONICS LETTERS, Associate Editor of the IEEE TRANSACTIONS ON POWER ELECTRONICS, and IEEE JOURNAL OF EMERGING AND SELECTED TOPICS IN POWER ELECTRONICS. He has received numerous industrial awards for his invented energy saving technologies.

Carl Ngai Man Ho (M'07–SM'12) received the B.Eng. and M.Eng. double degrees and the Ph.D. degree in electronic engineering from the City University of Hong Kong, Kowloon, Hong Kong, in 2002 and 2007, respectively. His Ph.D. research was focused on the development of dynamic voltage regulation and restoration technology.

From 2002 to 2003, he was a Research Assistant with the City University of Hong Kong. From 2003 to 2005, he was an Engineer with e.Energy Technology Ltd., Hong Kong. In 2007, he joined ABB Switzerland. He has been appointed as Scientist, Principal Scientist, Global Intellectual Property Coordinator and the last position was R&D Principal Engineer. He has led a research project team at ABB for three years to develop Solar Inverter technologies. In October 2014, he joined the University of Manitoba in Canada as an Assistant Professor and Canada Research Chair in Efficient Utilization of Electric Power. His research interests include Microgrid technologies, Renewable Energy interfaces, Real Time Digital Simulation technologies, and demand side control methodologies.

Dr. Ho is currently an Associate Editor of the IEEE TRANSACTIONS ON POWER ELECTRONICS and the IEEE JOURNAL OF EMERGING AND SELECTED TOPICS IN POWER ELECTRONICS.

Weimin Wu received the Ph.D. degree from the College of Electrical Engineering, Zhejiang University, Hangzhou, China, in 2005.

He worked as a Research Engineer in the Delta Power Electronic Center, Shanghai, from July, 2005 to June, 2006. Since July, 2006, he has been a Faculty Member at Shanghai Maritime University, where he is currently a Full Professor in Department of Electrical Engineering. He was a Visiting Professor in the Center for Power Electronics Systems, Virginia Polytechnic Institute and State University, Blacksburg, from September, 2008 to March, 2009. From November, 2011 to January, 2014, he was also a Visiting Professor in the Department of Energy Technology, working at the Center of Reliable Power Electronics. He has coauthored more than 80 papers and holds five patents. His areas of interests include power converters for renewable energy systems, power quality, smart grid, and energy storage technology.